

JET-POWERED MOLECULAR HYDROGEN EMISSION FROM RADIO GALAXIES

PATRICK OGLE¹, FRANCOIS BOULANGER², PIERRE GUILLARD¹, DANIEL A. EVANS³, ROBERT ANTONUCCI⁴, P. N. APPLETON⁵, NICOLE NESVADBA², & CHRISTIAN LEIPSKI⁶

¹Spitzer Science Center, California Institute of Technology, Mail Code 220-6, Pasadena, CA 91125

²Institut d'Astrophysique Spatiale, Universite Paris Sud, Bat. 121, 91405 Orsay Cedex, France

³MIT Center for Space Research, Cambridge, MA 02139

⁴Physics Dept., University of California, Santa Barbara, CA 93106

⁵NASA Herschel Science Center, California Institute of Technology, Mail Code 100-22, Pasadena, CA 91125 and

⁶Max-Planck Institut für Astronomie (MPIA), Königstuhl 17, D-69117 Heidelberg, Germany

Draft version October 30, 2018

ABSTRACT

H₂ pure-rotational emission lines are detected from warm (100-1500 K) molecular gas in 17/55 (31% of) radio galaxies at redshift $z < 0.22$ observed with the *Spitzer* IR Spectrograph. The summed H₂ 0-0 S(0)-S(3) line luminosities are $L(\text{H}_2) = 7 \times 10^{38} - 2 \times 10^{42}$ erg s⁻¹, yielding warm H₂ masses up to $2 \times 10^{10} M_{\odot}$. These radio galaxies, of both FR radio morphological types, help to firmly establish the new class of radio-selected molecular hydrogen emission galaxies (radio MOHEGs). MOHEGs have extremely large H₂ to 7.7 μm PAH emission ratios: $L(\text{H}_2)/L(\text{PAH}7.7) = 0.04 - 4$, up to a factor 300 greater than the median value for normal star-forming galaxies. In spite of large H₂ masses, MOHEGs appear to be inefficient at forming stars, perhaps because the molecular gas is kinematically unsettled and turbulent. Low-luminosity mid-IR continuum emission together with low-ionization emission line spectra indicate low-luminosity AGNs in all but 3 radio MOHEGs. The AGN X-ray emission measured with *Chandra* is not luminous enough to power the H₂ emission from MOHEGs. Nearly all radio MOHEGs belong to clusters or close pairs, including 4 cool core clusters (Perseus, Hydra, A 2052, and A 2199). We suggest that the H₂ in radio MOHEGs is delivered in galaxy collisions or cooling flows, then heated by radio jet feedback in the form of kinetic energy dissipation by shocks or cosmic rays.

Subject headings: galaxies: active, galaxies: quasars, galaxies: jets, infrared: galaxies

1. INTRODUCTION

1.1. AGN Radio Jet Feedback

AGN feedback on the interstellar and intracluster media (ISM and ICM) is thought to be an important factor regulating gas accretion, star formation, and AGN activity in galaxies (Granato et al. 2004; Scannapieco & Oh 2004; Hopkins et al. 2006; Croton et al. 2006; Ciotti & Ostriker 2007; Merloni & Heinz 2008). This may occur through either a sub-relativistic wind in radio-quiet quasars or a relativistic radio jet in the case of radio-loud quasars and radio galaxies. In the latter case, the kinetic energy of the jet integrated over its lifetime is typically more than enough to unbind the ISM of even the most massive galaxy. While much effort has been devoted to simulating the impact of jets on the hot ICM (e.g., Zanni et al. 2005), less is known about the jet-ISM interaction. Recent simulations have shown that a radio jet may couple strongly to an inhomogeneous, clumpy ISM until the radio lobes break free into intergalactic space (Sutherland & Bicknell 2007). In this process, the jet drives radiative shocks into dense clumps but does not ablate them, while less dense gas may be ablated and advected to larger radii. While such detailed simulations have been made of the impact of jets on the atomic and ionized components of the ISM, the impact on the molecular gas phase has not been considered in any detail.

Ogle et al. (2007) found that the mid-IR spectrum of radio galaxy 3C 326 N displays high-luminosity H₂ emission, coupled with weak PAH emission indicative of a low star formation rate. We presented evidence that 3C 326 N belongs to an interacting galaxy pair and suggested that the copious warm H₂ is heated by accretion from the companion 3C 326 S. Further investigation revealed the presence of fast neutral gas outflow, possibly driven by the radio jet (Nesvadba et al. 2010). Therefore, a strong interaction between the radio jet and molecular gas, rather than accretion, may power the H₂ emission.

H₂ emission may prove to be a key in understanding how radio jet feedback impacts the molecular gas phase and thereby suppresses star formation in massive galaxies. The most likely H₂ heating mechanism is jet-driven shocks in a multiphase interstellar medium. Cosmic ray heating and X-ray emission from the AGN are alternative heating mechanisms that we will consider.

1.2. H₂ Emission from Galaxies

Rotational and ro-vibrational H₂ transitions are important cooling channels for warm molecular gas, observed as a series of infrared emission lines. These transitions are highly forbidden because of the zero permanent dipole moment of H₂. In normal star-forming galaxies with total H₂ to total (3-1100 μm) IR ratios $L(\text{H}_2)/L_{\text{TIR}} < 0.001$, these lines are thought to be emitted by stellar photodissociation regions (Rigopoulou et al. 2002; Higdon et al. 2006; Roussel et al. 2007).

Much stronger molecular hydrogen emission galax-

ies (MOHEGs) with $L(\text{H}_2)/L_{\text{TIR}} > 0.001 - 0.1$ have been revealed by recent *Spitzer* observations (Ogle et al. 2007). Extreme H_2 emission has been found in a variety of galaxy types so far, including luminous infrared galaxies (Lutz et al. 2003), colliding galaxies (Appleton et al. 2006), central dominant cluster galaxies (Egami et al. 2006; De Messieres et al. 2009), and radio galaxies (Ogle et al. 2007; Willett et al. 2010). Enhanced H_2 emission has been observed in AGNs with ISO (Rigopoulou et al. 2002), and more recently from AGNs in the *Spitzer* SINGS survey (Roussel et al. 2007). Relatively strong H_2 emission is also seen in PG quasars with strong PAH emission (Schweitzer et al. 2006; Veilleux et al. 2009). AGN X-ray heating or shocks have been cited as possible ways to power the H_2 emission.

The first galaxy discovered with strong ro-vibrational and rotational H_2 lines ($2 \times 10^{42} \text{ erg s}^{-1}$) is the luminous infrared galaxy (LIRG) NGC 6240 (Joseph & Wright 1984; Lutz et al. 2003; Armus et al. 2006). Keck Adaptive Optics and HST NICMOS imaging in near-IR H_2 ro-vibrational lines reveal a complex network of hot molecular gas filaments embedded in a larger network of $\text{H}\alpha$ emission (Max et al. 2005). This galaxy has a binary active nucleus (Komossa et al. 2003) and is thought to be a late stage major merger of two gas-rich spiral galaxies. Shock-heating driven by the merger may power the strong H_2 emission spectrum.

Appleton et al. (2006) find high luminosity H_2 emission from an intergalactic shock between colliding galaxies in Stephan’s Quintet. The X-ray emission from the shock, though conspicuous, is too weak to power the H_2 lines. Instead, it is likely that the H_2 emission is powered by kinetic energy dissipation through turbulence in a multi-phase post-shock layer (Guillard et al. 2009). In this case the H_2 emission provides ten times the luminosity of the next brightest Mid-IR line [Si II], demonstrating that it is likely the dominant coolant in this group-wide shock (Cluver et al. 2010).

H_2 ro-vibrational emission from 1000-2000 K molecular gas is seen from the brightest central galaxies in some galaxy clusters (Donahue et al. 2000). *Spitzer* observations have shown these galaxies also display rotational lines from H_2 at lower (100-1500 K) temperatures (Egami et al. 2006; Johnstone et al. 2007). The warm molecular gas is often associated with extended optical emission line filaments. Extensive networks of such filaments are found in 30-50% of X-ray luminous, rich galaxy clusters, associated with the central-dominant (cD) galaxy (Lynds 1970; Heckman et al. 1981; Cowie et al. 1983; Johnstone et al. 1987; Heckman et al. 1989; Crawford et al. 1999).

The origin, confinement, and excitation mechanism for cluster emission line filaments are longstanding mysteries (Minkowski 1957; Burbidge & Burbidge 1965). The filaments in Perseus A may be formed in-situ by the interaction of the radio lobes with the hot intra-cluster medium (Conselice et al. 2001). Since the filaments are dusty and have near-solar metal abundances, it is more likely that they are composed of cool gas dredged up by the radio jet from the center of the galaxy (Churazov et al. 2000; Ferland et al. 2009). Galaxy collisions and ram-pressure stripping are two other ways

to create intracluster filaments of atomic and molecular gas (Kenney et al. 2008; Sivanandam et al. 2010).

The gas filaments surrounding Per A are ~ 100 times more luminous than expected from a cooling flow and therefore must be powered externally (Cowie et al. 1983). The $\text{H}\alpha$ filaments consist of extremely narrow threads, most likely confined by a magnetic field (Fabian et al. 2008). Kinetic energy dissipation by magnetohydrodynamic (MHD) shocks or dissipative MHD waves driven by the radio lobes may power the atomic and molecular emission line spectra (Kent & Sargent 1979; Heckman et al. 1989; Hatch et al. 2005; Guillard et al. 2009). Molecular gas heating by cosmic rays has also been suggested (Ferland et al. 2008, 2009), and may help to explain some anomalous atomic forbidden emission line ratios.

1.3. Overview

We present a large *Spitzer* spectroscopic survey of 55 radio galaxies. We find a large number of H_2 luminous galaxies (17), which belong to and further define the MOHEG class. We use mid-IR and optical forbidden lines, aromatic features, and $24 \mu\text{m}$ continuum emission to investigate the gas and dust content and H_2 power source in these radio-selected MOHEGs. We describe the radio galaxy sample, observations, and spectra in Sections 2-4. We estimate warm H_2 masses using excitation diagrams in Section 5. We explore the dust emission properties of the sample in Sections 6 and 7. We discuss the H_2 /PAH diagnostic ratio and use this to redefine the MOHEG class in Sections 8 and 9. We estimate star formation rates and use ionic forbidden line ratios to diagnose AGN activity in Sections 10 and 11. We use *Chandra* observations to rule out X-ray heating by the AGN in Section 12. The host galaxy morphologies and environments are discussed in Section 13. Radio jet morphologies are considered in Section 14. Finally, we discuss evidence in support of radio jet feedback in Section 15.1, cosmic ray heating in Section 15.2, and the origin of the molecular gas in Section 15.3.

2. SAMPLE

We conducted a survey of Fanaroff & Riley (1974) class-II radio galaxies and quasars from the 3CRR catalog with the *Spitzer* IRS (Ogle, Whysong, & Antonucci 2006) and a similar survey of FR I radio galaxies (Leipski et al. 2009). The FR II galaxies were selected from the 3CRR catalog to form a redshift and flux-limited sample with $z < 1$ and $S_\nu(178 \text{ MHz}) > 16.4 \text{ Jy}$. The FR I galaxies form a representative (yet incomplete) sample at $z < 0.13$, selected from the 3CR catalog with a flux limit of $S_\nu(178 \text{ MHz}) > 15 \text{ Jy}$.

From the above two samples, we selected all 23 FR I galaxies and the subsample of 19 FR II galaxies at $z < 0.22$. We excluded the blazars BL Lac and 3C 371, which have mid-IR spectra completely dominated by synchrotron emission, and the radio-intermediate quasar E1821+643. We retrieved the data for 8 additional FR II and 5 FR I radio galaxies in the *Spitzer* archive, for a total of 27 FR II and 28 FR I galaxies at $z < 0.22$. The redshift limit of $z < 0.22$ ensures that the full H_2 S(0)-S(7) line series falls in the *Spitzer* IRS wave band.

The radio galaxy sample is presented in Tables 1 and 2. Alternate names, host galaxy properties, cluster mem-

bership, and interaction signatures are listed in Table 3 for H_2 detected radio galaxies. Throughout this paper we assume a cosmology with Hubble constant $H_0 = 70 \text{ km s}^{-1} \text{ Mpc}^{-1}$, matter density parameter $\Omega = 0.3$, and dark energy density $\Omega_\Lambda = 0.7$.

3. OBSERVATIONS

3.1. *Spitzer*

The radio galaxies in Tables 1 and 2 were observed with the *Spitzer* IR Spectrograph (IRS; Houck et al. 2004). Spectra were taken with the low-resolution ($R \sim 60\text{--}120$) modules Short-Low 2 (SL2), Short-Low 1 (SL1), Long-Low 2 (LL2), and Long-Low 1 (LL1) over the wavelength range $5\text{--}36.5 \mu\text{m}$. At the galaxy redshifts of 0.002–0.22, $1''0$ corresponds to $0.04\text{--}3.6 \text{ kpc}$. The slit widths are $3''6$, $3''7$, $10''5$, and $10''7$, respectively, corresponding to $0.15\text{--}13 \text{ kpc}$ for SL and $0.42\text{--}38 \text{ kpc}$ for LL. The telescope was nodded to place the nucleus of each galaxy at the $1/3$ and $2/3$ positions along each slit.

We began our analysis with the S15–S17 pipeline processed, basic calibrated data sets (BCDs). Off-slit observations were subtracted to remove background light. Spectra were extracted (using SPICE 2.1) within tapered regions matching the *Spitzer* point-spread function and including the first Airy ring (SL2: $7''2$ at $6 \mu\text{m}$, SL1: $14''4$ at $12 \mu\text{m}$, LL2: $21''7$ at $16 \mu\text{m}$, LL1: $36''6$ at $27 \mu\text{m}$). We tried both regular and optimal extraction within these regions (Narron et al. 2007), and selected the extraction with higher signal-to-noise for further analysis. For unresolved sources, the continuum and emission line fluxes from regular and optimal extractions are in agreement.

The flux uncertainties produced by the *Spitzer* pipeline are known to be too large for faint sources. The pipeline (versions S18.7 and earlier) does not properly adjust the uncertainties for ‘droop’, a systematic, additive effect which is proportional to the total photocurrent incident upon the detector. We divided flux uncertainties for each spectral order by a constant factor of 0.3–2.1, to better reflect the observed noise characteristics. The uncertainty scale factor for each order was determined from the ratio of the mean pipeline uncertainties to the observed noise in emission line-free regions.

Spectral orders with low flux were adjusted upwards by factors of 1.0–2.0 to correct for interorder slit loss differences. Such differences may arise from pointing inaccuracies, even for unresolved sources. The differences in slit widths and wavelength-dependent extraction apertures may also lead to mismatches in continuum or line flux between orders for spatially resolved sources. Our spectral order matching will properly correct for this effect in the case that the extended continuum and line emission are cospatial and have similar spectra, such as might be the case for extended star-forming regions. However, the emission line equivalent widths and line flux ratios between orders could be off by as much as the interorder correction factor (< 2.0) in the case of extended nebular or H_2 emission. This should not be an issue for any galaxies except Per A, 3C 293, and Cen A, the only ones where the emission lines and PAH features appear to be spatially extended along the spectrograph slits. For all other sources, the mid-IR (MIR) emission (including the H_2 emission) is unresolved and resides within the central 2–40 kpc of the host galaxies.

We measured the emission line and PAH features of all galaxies in a systematic way using the spectral fitting tool PAHFIT (Smith et al. 2007). The continuum is modeled with a sum of starlight and thermal (black-body) emission components, absorbed by a uniform dust screen. This is intended only as an empirical description of the continuum, not a physical model. The spectrally resolved PAH features are fit by Drude profiles. The unresolved H_2 and forbidden atomic emission lines are fit by Gaussian profiles. Emission line and PAH fluxes from the galaxies are presented in Tables 4–8. We also measured narrow-band $24 \mu\text{m}$ fluxes (3.7σ -clipped average over $22.5\text{--}25.5 \mu\text{m}$ rest; Tables 1–2) from the IRS spectra and used them to estimate mid-IR continuum luminosities (Table 9).

In principle, the continuum for each source should be fit with a dust radiative transfer model, but this is outside the scope of the present work. Instead, we tailored the continuum model in two cases where the simple multi-temperature black body plus screen extinction model did not work. For Perseus A, we added silicate emission features to the continuum. We introduced the capability to fit optically thin silicate emission features with PAHFIT, computing the silicate emission as black-body emission multiplied by an empirical dust extinction curve. In the Cygnus A spectrum, $18 \mu\text{m}$ silicate absorption is unusually weak or absent relative to the $9 \mu\text{m}$ silicate absorption, perhaps because of radiative transfer effects. Therefore we removed the $18 \mu\text{m}$ silicate absorption feature from the Chiar & Tielens (2006) Galactic center extinction curve in order to model the absorption.

3.2. *Chandra*

In order to test the possibility of H_2 heating by X-rays from AGN, we compiled unabsorbed 2–10 keV nuclear X-ray luminosities measured by *Chandra* (Table 9). For several sources without published X-ray luminosities, we used archival *Chandra* data to measure them ourselves (Table 10). We reprocessed the *Chandra* data using CIAO v4.1.2 with the CALDB v4.1.2 to create a new level-2 events file filtered for the grades 0, 2, 3, 4, and 6 and with the $0.5''$ pixel randomization removed. To check for periods of high background, we extracted light curves for the chip on which the source was placed, excluding point sources. Few periods of high background were found in any observation, and so we used almost all available data in our analysis.

We extracted the nuclear spectra for each source from a small circle (typically of radius 5 pixels or $2.5''$), and sampled background from an adjacent region free from point sources. In most cases, the point-like emission from the nucleus was easily separated from any extended emission components, though there may be significant contamination from the surrounding hot cluster gas in the case of the Zw3146 BCG. We do not consider the possibility of H_2 heating by X-ray emission from the extended intracluster medium or X-ray emission from the extended radio source.

We adopted the standard X-ray spectral models for radio-loud AGN described by Evans et al. (2006) to fit each spectrum. In the case of narrow-line radio galaxies (NLRGs), the canonical model takes the form of the combination of a heavily absorbed power law and a soft, unabsorbed power law that Evans et al. (2006) inter-

puted to originate at the base of an unresolved jet. In Table 10 we present an observation log and summarize the best-fitting models for each source.

4. H₂ SURVEY RESULTS AND SPECTRA

We detect two or more H₂ emission lines from 17/55 (31%) of the radio galaxies in our sample (Table 4). We require $> 2.5\sigma$ detection of 2 lines at the systemic redshift. A typical 2σ H₂ S(1) detection limit for the sample is 8×10^{-16} erg s⁻¹ cm⁻² (8×10^{-19} W m⁻²), but this may vary with redshift and H₂ line contrast relative to the continuum.

H₂ line and PAH fluxes for galaxies with only one or no H₂ lines detected are presented in Table 6. Upper limits to their H₂ luminosities are estimated as $L_{\text{H}_2} < 1.6L[\text{H}_2 \text{ 0-0 S(1)+ S(3)}]$, where the correction factor 1.6 accounts for the S(0) + S(2) line flux and is the mean value of $[\text{H}_2 \text{ S(0) + S(1) + S(2) + S(3)}]/[\text{H}_2 \text{ S(1) + S(3)}]$ for galaxies where all 4 lines were detected. We use this rather than the sum of 4 upper limits for S(1) through S(4), which would be an overestimate.

The *Spitzer* IRS spectra of the H₂ detections are presented in Figures 1-7, along with archival HST optical images for most sources. Some of these spectra were previously presented by Ogle, Whysong, & Antonucci (2006), Ogle et al. (2007), and Leipski et al. (2009), but we show them here as well for completeness. The Cen A spectrum was originally presented by Weedman et al. (2005). H₂ pure-rotational lines, forbidden lines of O, Ne, Si, S, Ar, Cl, and Fe, and polycyclic aromatic hydrocarbon (PAH) features are seen in many of the spectra (Tables 4-8). Galaxies with large 7.7 μm PAH equivalent width are presented in Figure 1 and those with small 7.7 μm PAH equivalent width in Figures 2-3. The mid-IR luminous radio galaxies Per A, Cyg A, 3C 433, and 3C 436, which contain dust-obscured quasars, are presented in Figure 4. The H₂ emission is difficult to see on top of the continuum emission from the galactic nuclei in some spectra. However, subtraction of a continuum model clearly reveals the H₂, PAH, and other emission lines (Per A, Cyg A, and Cen A Figs. 5-7).

5. H₂ LUMINOSITIES, TEMPERATURES, MASSES, AND SURFACE DENSITIES

In order to compute the mass of warm molecular gas, it is first necessary to know the H₂ excitation mechanism. The low critical densities (H₂-H₂ $n_{\text{crit}} < 10^3$ cm⁻³ at $T > 100$ K) of the H₂ 0-0 S(0) and S(1) emission lines (Le Bourlot et al. 1999; Wrathmall et al. 2007) ensure that their upper levels will be collisionally excited in almost any environment where warm H₂ is found. Non-thermal excitation by UV photons or cosmic-ray secondary electrons (Ferland et al. 2008) may contribute to the higher rotational and ro-vibrational levels, but are inefficient at exciting the lower pure-rotational levels. Therefore the lowest H₂ energy levels, which dominate the warm H₂ mass budget, must be in thermal equilibrium.

Assuming thermal equilibrium in gas at a single temperature T , the H₂ luminosity is determined by the H₂ mass M_{H_2} and T according to

$$L(\text{H}_2) = \frac{M_{\text{H}_2}}{2m_p} l_{\text{H}_2}(T)$$

where the mean luminosity of a single H₂ molecule, summed over all transitions $u \rightarrow l$ is

$$l(\text{H}_2) = \sum_{u,l} h\nu_{ul} A_{ul} f_u(T)$$

The occupation number $f_u(T)$ of each level is determined by the Boltzmann factor and partition function. For example, a molecular gas mass of $M_9 = M_{\text{H}_2}/10^9 M_\odot$ and a temperature of 200 K gives

$$L(\text{H}_2) = 1.1 \times 10^{42} \text{ erg s}^{-1} M_9$$

For multiple temperature components, the luminosity of each component can be computed separately.

For all radio galaxies with two or more H₂ emission lines detected, we construct excitation diagrams to determine the temperature distribution and mass of H₂. For the limiting case of an H₂ source size of $3''.7 \times 3''.7$ uniformly filling the width of the SL slit, we plot the column density of the upper level divided by the statistical weight for each transition (Figs. 8-10).

We simultaneously fit the data with 3 temperature components (Table 11), the minimum number necessary to fit the emission line fluxes and parameterize what is likely a continuous temperature distribution. We quote 1σ single parameter uncertainties for the H₂ temperatures and masses. Upper limits are included in the fits as 2σ detections with 1σ errorbars. This allows us to give conservative upper limits for the lowest temperature component for sources where the S(0) line is not detected, without affecting much the other components. Note that the lowest temperature component, which is constrained by the S(0) and S(1) lines dominates the total H₂ mass. We give an upper limit for the warmest temperature component mass in 3C 338, where the S(6) and S(7) lines are not detected.

We assume that the H₂ level populations and ratios of ortho/para H₂ are in local thermodynamic equilibrium (LTE) and adjust the statistical weights of the ortho transitions iteratively to obtain a self-consistent fit. There is no evidence for non-equilibrium ortho/para ratios, which would manifest as suppressed or enhanced emission from odd- J relative to even- J transitions. The ortho/para ratios may depend upon the detailed thermal history of the gas, and can take much longer than the gas cooling time ($\sim 10^4$ yr) to reach their equilibrium values (Wilgenbus et al. 2000). However, for the warm ($T > 100$ K) H₂ observed by *Spitzer*, the equilibrium ortho/para ratio takes on a narrow range of values (1.6-3.0) such that the equilibrium assumption has only minor consequences for our model fits. For example, assuming an ortho/para ratio of 3.0 rather than 2.1 decreases the temperature of the coolest H₂ component in 3C 326 from 110 to 100 K, and raises the mass by only 27% to $2.8 \pm 0.6 \times 10^9 M_\odot$.

To determine the sensitivity of our model fits to the number of temperature components, we tried both 2-component and 3-component fits to all of the lines in the 3C 326 N excitation diagram. The 2-component fit gives a mass of $8.7 \pm 3.2 \times 10^8 M_\odot$ at 140 K ($\chi^2/\text{DOF} = 36.6$), compared to $2.2 \pm 1.2 \times 10^9 M_\odot$ at 110 K ($\chi^2/\text{DOF} = 1.8$) for the 3-component fit. The 3-component fit has much smaller residuals and is clearly better. The additional temperature component increases the estimated H₂ mass by a factor of 2.5 in this case. Which lines are detected and used in the fit can also change the estimated H₂ mass. If we throw out the S(5), S(6), and S(7) lines and refit the 2 component model, we find $1.6 \pm 0.7 \times 10^9 M_\odot$ at 120 K ($\chi^2/\text{DOF} = 1.9$).

We measure radio galaxy warm H_2 masses from $8 \times 10^6 M_\odot$ up to an amazing $2 \times 10^{10} M_\odot$, the bulk at temperatures of 100-200 K (Tables 11 and 12). Such large H_2 masses imply the wholesale heating of an entire galaxy's worth of molecular gas in some cases. Smaller masses ($3 \times 10^4 - 8 \times 10^7 M_\odot$) of warmer H_2 at 200-1500 K are also found in all galaxies where H_2 is detected. Comparable luminosity is emitted by each temperature component in a given galaxy, though most of the mass resides in the coolest component (Table 11). In all cases where there are several high-level lines detected, the H_2 temperature increases with upper-level excitation temperature. This produces the characteristic curves in Figures 8-10, which have less negative slopes at higher energies. This behavior is also seen in the excitation diagram for the Perseus A filaments (Johnstone et al. 2007). This is expected for any astrophysical situation where there is a range of temperatures and densities present (Ferland et al. 2008).

The total warm H_2 column densities and column density lower limits range from $< 4 \times 10^{20} - 1 \times 10^{23} \text{ cm}^{-2}$ ($3 - 800 M_\odot \text{ pc}^{-2}$). Only lower limits can be inferred for spatially unresolved H_2 emission. This spans the range observed for normal star-forming galaxies at the low end to ULIRGs at the high end (Gracia-Carpio et al. 2007).

CO emission has been detected by past observations (Evans et al. 1999; Lim et al. 2003; Salome & Combes 2003; Evans et al. 2005; Okuda et al. 2005; Salome et al. 2006; Saripalli & Mack 2007; Israel et al. 1990; Nesvadba et al. 2010; Ocana Flacquer et al. 2010) of several radio MOHEGs (Table 12). The mass of cold (10 – 50 K) H_2 estimated assuming the standard Galactic CO to H_2 conversion factor of $4.6 M_\odot / (\text{K km s}^{-1} \text{ pc}^2)$ ranges from $4 \times 10^6 - 2 \times 10^{10} M_\odot$. However, we caution that the applicability of the Galactic conversion factor to the extreme conditions in radio MOHEGs has not been established. This caveat notwithstanding, the inferred ratio of warm ($T > 100 \text{ K}$) to cold H_2 in these galaxies ranges from $< 0.18-2.1$. The galaxies 3C 218, 272.1, 326, 424, and 433 are particularly remarkable in having warm/cold H_2 ratios of > 0.5 . A large fraction of the H_2 in these galaxies is disturbed and heated to temperatures $> 100 \text{ K}$.

6. 24 μM DUST EMISSION

The formation and shielding of H_2 requires the presence of dust, which may reveal itself through IR continuum and PAH emission features (Guillard et al. 2010). However, there must be a sufficient UV radiation field to heat the very small dust grains (VSGs) and excite the PAH stretching or bending modes in order to observe mid-IR dust signatures. A UV photon field may be sustained by 1) star formation, 2) AGN emission, or 3) thermal bremsstrahlung and line emission from radiative shocks (Dopita & Sutherland 1996). It must be kept in mind that the H_2 , VSG, and PAH emission regions are spatially unresolved and may or may not be coincident. Also, different types of sources can contribute in different ratios to each of these spectral features.

First we consider the ratio of H_2 to 24 μm dust emission (Fig. 11) for star-forming galaxies (Roussel et al. 2007). There is a trend (with large scatter) for $L(H_2)/L_{24}$ to decrease with L_{24} . ULIRGs (Higdon et al. 2006) have smaller $L(H_2)/L_{24}$ than nearby spirals and dwarfs, by a

factor of ~ 5 . This is similar to the known trend of decreasing $L(\text{PAH})/L_{24}$ with L_{24} observed for starbursts and ULIRGs (Desai et al. 2006; Tran et al. 2001, and Fig. 12). It is debated whether this latter trend is intrinsic to star-forming regions or whether it reflects an increasing AGN contribution to the continuum at higher luminosity. In either case, the tendency of H_2 and PAH emission to decrease together relative to L_{24} may suggest that they are both powered by star formation in starbursts and ULIRGs. On the other hand, Zakamska (2010) finds that H_2 emission is less obscured than PAH emission in ULIRGs, indicating a different spatial distribution.

The radio galaxies in our sample have up to 20 times larger ratio of $L(H_2)/L_{24}$ than do normal star-forming galaxies (Fig. 11). In some cases (e.g., 3C 326 and Stephan's Quintet), $> 10\%$ of the bolometric IR luminosity comes out in the H_2 lines (Ogle et al. 2007). This dramatically indicates that the H_2 emission is not powered by star formation, and that H_2 emission is an important and perhaps primary coolant for the ISM in these sources. Strong H_2 emission is often an indicator of magnetic (C-type) shocks in Galactic sources such as Herbig-Haro jets (Neufeld et al. 2006) and supernovae (Cesarsky et al. 1999; Neufeld et al. 2007). A deficit of 24 μm continuum relative to H_2 emission indicates the importance of non-radiative (e.g., shock) heating.

The SINGS AGNs also have enhanced $L(H_2)/L_{24}$ (Roussel et al. 2007), though they are not as well separated from the star-forming galaxy locus as radio galaxies (Fig. 11). Non-radiative heating of H_2 appears to be important in these nearby, radio-quiet AGNs. A similar enhancement in $L(H_2)/L_{24}$ is seen for some of the Kaneda et al. (2008) 'dusty ellipticals', which are RSA ellipticals detected by IRAS (Goudfrooij & de Jong 1995). Interestingly, 12/14 of the H_2 detected ellipticals in the Kaneda et al. (2008) sample have radio sources detected in the NVSS or SUMSS survey-7 compact sources and 5 FR Is. Radio jet activity could be responsible for exciting the excess H_2 emission in these sources.

7. PAH EMISSION

PAH emission features are detected in all of the radio MOHEGs except Cyg A (Table 5) and in half of the H_2 nondetected radio galaxies (Table 6). However, the ratio of 7.7 μm PAH to 24 μm continuum emission $L(\text{PAH}7.7)/L_{24}$ is generally lower by a factor of 10-100 compared to normal star-forming galaxies from the SINGS sample (Fig. 12). The mid-IR continuum of most radio galaxies and radio MOHEGs is therefore not star-formation dominated. In many of these galaxies, the continuum has been shown to be AGN dominated, including contributions from AGN-heated dust and synchrotron emission from the jet (Ogle, Whyson, & Antonucci 2006; Cleary et al. 2007; Tadhunter et al. 2007; Haas et al. 2008; Leipski et al. 2009).

The large scatter that we see in $L(\text{PAH}7.7)/L_{24}$ (2 dex) primarily reflects varying star formation vs. AGN fractional contributions to the spectra. Additional scatter is introduced by variation in the 7.7/11.3 μm PAH band ratio (Fig. 13). Low $L(\text{PAH}7.7)/L_{24}$ is also observed in the Kaneda et al. (2008) dusty ellipticals, indicating

that the warm dust continuum in these sources does not come from star formation.

The median PAH(6.2 μm)/PAH(7.7 μm) ratio is 0.25 for radio MOHEGs, which is indistinguishable from the median ratio (0.28) for normal star-forming SINGS galaxies (Fig. 13). The median PAH(7.7 μm)/PAH(11.3 μm) ratio of 1.8 is significantly lower in radio MOHEGs than the median value of 4.1 measured in star-forming SINGS galaxies and within the range of values reported for SINGS AGNs (Smith et al. 2007). The Kaneda et al. (2008) dusty elliptical galaxies have a similar median 7.7 to 11.3 μm band ratio of 1.4. Smith et al. (2007) present an extensive discussion of possible interpretations of the observed differences in 7.7 to 11.3 μm band ratio between AGNs and star-forming galaxies and among AGNs.

The impact of the PAH ionization state and size distribution on PAH emission spectra has been quantified in models (Bakes et al. 2001; Draine & Li 2001; Flagey et al. 2006). In these models, the 7.7 to 11.3 μm band ratio is mainly sensitive to the ionization state and is lower for neutral PAHs than for cations. This interpretation is supported by observations of photodissociation regions (PDRs) which show that the 7.7 to 11.3 μm band ratio decreases with increasing depth into the cloud (Rapacioli et al. 2005). The ionization states of PAHs depend on the PAH ionization parameter $G_{UV} \times T_e^{0.5}/n_e$, where G_{UV} is the $912 < \lambda < 2400 \text{ \AA}$ UV field energy density relative to the Solar Neighborhood value (Habing 1968), and T_e and n_e the temperature and electron density. The electron density is that of the neutral, molecular, and atomic gas where PAHs are present.

The interpretation of Galactic data leads to equal fractions of neutral and cation PAHs in the diffuse Galactic ISM for a mean ionization parameter $\sim 1000 \text{ K}^{0.5} \text{ cm}^3$ and a 7.7 to 11.3 μm band ratio (measured with PAHFIT) of 2.9 ± 0.2 (Flagey et al. 2006). The median value of the 7.7 to 11.3 μm band ratio of radio MOHEGs (1.8) is smaller than the value for the Galactic diffuse interstellar medium. This implies a smaller PAH ionization parameter, which could be accounted for by lower G_{UV} in galaxies with a low star formation rate, or by larger n_e from increased ionization by cosmic rays or X-rays.

In the Stephan's Quintet intergalactic shock, the observed PAH emission is consistent with the mass of warm H_2 gas heated by a radiation field with $G_{UV} = 1.4$, assuming a Galactic dust-to-gas mass ratio and a galactic dust size distribution (Guillard et al. 2010). This shows that PAHs can survive in dense regions of the interstellar medium which are shocked at velocities $< 100 \text{ km s}^{-1}$. PAHs could potentially be destroyed by faster shocks, which may be present in the diffuse ISM (Micelotta et al. 2010a). In the hot $10^6 - 10^7 \text{ K}$ X-ray emitting gas phase, PAHs would mostly be destroyed by electron collisions and would not survive more than a few 10^3 years (Micelotta et al. 2010b). PAHs are likely protected from electron sputtering in the denser, colder phases.

We similarly expect to see PAH emission from the large H_2 reservoir in radio MOHEGs, excited by the ambient UV radiation field. PAH destruction by X-rays may possibly reduce PAH abundances in the vicinity of the AGN (Voit 1991). However, the four radio MOHEGs with sig-

nificant star formation (discussed in §10–3C 31, 293, 315, and Hydra A) and correspondingly strong UV radiation field show nearly normal 7.7 and 11.3 μm PAH equivalent widths and PAH band ratios, demonstrating that PAH abundances have not been depleted by the AGNs on a galactic scale. The remaining radio MOHEGs show relatively weak PAH emission, consistent with a weaker UV field.

8. H_2 TO PAH EMISSION RATIO

We plot the ratio of H_2 luminosity in the 0-0 S(0)-S(3) lines over $L(\text{PAH7.7})$ versus L_{24} (Fig. 14). Normal star-forming galaxies from the SINGS survey (Roussel et al. 2007) have a median ratio $L(\text{H}_2)/L(\text{PAH7.7}) = 0.014$, which appears to be independent of L_{24} over four decades ($L_{24} = 10^6 - 10^{10} L_\odot$). The mean $L(\text{H}_2)/L(\text{PAH7.7})$ has a similar but slightly greater value for ULIRGs (Higdon et al. 2006; Desai et al. 2006).

In contrast, all of the H_2 detected radio galaxies have very large $L(\text{H}_2)/L(\text{PAH7.7}) = 0.03 - 4$ or greater. The most extreme sources, with $L(\text{H}_2)/L_{\text{PAH}} > 3$ are 3C 326 N (Ogle et al. 2007) and 3C 424. Other galaxies of different types, including the LIRG NGC 6240 (Lutz et al. 2003), the Zw 3146 BCG (Egami et al. 2006), and the Stephan's Quintet intergalactic shock (Appleton et al. 2006) are also unusual in having large $L(\text{H}_2)/L_{\text{PAH}}$ ratios. Strikingly, all of the SINGS Seyferts and all but 4 of the SINGs LINERs (Roussel et al. 2007) also stand out as having relatively large $L(\text{H}_2)/L_{\text{PAH}} = 0.02 - 0.2$, though not so large as the most extreme radio galaxies. Such large ratios indicate shock, cosmic ray, or X-ray heating rather than UV heating of the molecular gas phase (Rigopoulou et al. 2002; Roussel et al. 2007). We explore the various possible heating mechanisms for H_2 in radio galaxies below.

Alternatively, it might be argued that a high ratio $L(\text{H}_2)/L(\text{PAH7.7})$ is caused by a low abundance of PAHs in the warm molecular gas rather than low UV field. A UV field of $G_{UV} \sim 4$ would be required explain the 11.3 μm PAH flux from 3C 326 N if it is associated with the observed warm H_2 and CO (Nesvadba et al. 2010), assuming a normal H_2/CO conversion factor (Table 12). We use archival GALEX UV data to independently constrain the intensity of the radiation field and PAH abundance. The NUV AB magnitude is 21.47, which translates into a surface brightness of $1.59 \times 10^{-6} \text{ W m}^{-2} \text{ sr}^{-1}$, assuming emission from star-forming regions uniformly covering a 5 arcsec (8 kpc) diameter area. This corresponds to a mean UV radiation field $G_{UV} = 12$. If any of the observed UV radiation comes from the AGN, the G_{UV} value contributing to PAH excitation would be less. A comparison of the two G_{UV} estimates gives an upper limit on the PAH depletion of ~ 3 . This is far from sufficient to explain the extreme ratio $L(\text{H}_2)/L(\text{PAH7.7}) > 4$ in 3C 326 N, which is 300 times the mean value in normal star-forming galaxies.

9. MOHEG DEFINITION

Since we do not have far-IR measurements for most of the sources in our sample, we do not use our original MOHEG definition (Ogle et al. 2007). We could re-express that definition as $L(\text{H}_2)/L_{24} > 2 \times 10^{-2}$ (dashed line in Fig. 11), excluding all normal star-forming galaxies from the MOHEG class. The observed H_2 to continuum con-

trast ratio for our H₂ detected radio galaxy sample ranges from $L(\text{H}_2)/L_{24} = 6 \times 10^{-4} - 0.4$, which means that only 9/17 of these galaxies would be considered MOHEGs by such a definition. Inspection of Figure 11 suggests that defining MOHEGs in terms of a minimum $L(\text{H}_2)/L_{24}$ contrast ratio is problematic. For one, this ratio decreases with L_{24} for normal star-forming galaxies, so a line with negative slope in that figure would do a better job at separating MOHEGs. However, it would not completely account for the variation in AGN continuum contribution at 24 μm , which introduces scatter into this relation.

The much cleaner separation between MOHEGs and normal star-forming galaxies in Figure 14 compared to Figure 11 motivates us to redefine MOHEGs as galaxies with $L(\text{H}_2)/L(\text{PAH}7.7) > 0.04$. This particular cutoff was chosen to exclude all non-AGN SINGs galaxies from the MOHEG class. With our new definition, 16/17 of the H₂ detected radio galaxies, 10/18 of the Kaneda et al. (2008) dusty ellipticals, NGC 6240, and the Zw 3146 BCG are all MOHEGs. We call radio galaxies that are MOHEGs ‘radio MOHEGs’ to distinguish them from MOHEG samples selected in other wavebands. The radio galaxy 3C 31, with $L(\text{H}_2)/L(\text{PAH}7.7) = 0.03$ falls just below the MOHEG cutoff as a result of the relatively large contribution of star formation and strong 7.7 μm PAH emission its mid-IR spectrum (Fig. 1). However, for simplicity and since it has a larger $L(\text{H}_2)/L(\text{PAH}7.7)$ ratio than any SINGs galaxy of similar luminosity L_{24} , we will also call this source a radio MOHEG. It is not possible with the current data to reliably classify the H₂ nondetected radio galaxies with respect to the MOHEG criterion. Therefore, the 31% MOHEG fraction in our radio galaxy sample should be considered a lower limit.

The success of the $L(\text{H}_2)/L(\text{PAH}7.7)$ diagnostic ratio in distinguishing between AGN and star-formation dominated spectra reflects the different molecular gas heating mechanisms in the two classes. Furthermore, the $L(\text{H}_2)/L(\text{PAH}7.7)$ value at a given L_{24} might be used to determine the ratio of AGN to star-forming contributions to these two emission features. If the H₂ and 7.7 μm PAH emission have different spatial extent, this ratio and classification as a MOHEG might depend upon the aperture used to extract the spectrum. There is a similar issue with AGN optical classification, since AGN fraction tends to increase with decreasing aperture size.

10. STAR FORMATION

In general, 3C radio galaxies tend to have less luminous PAH emission and lower inferred star-formation rates than other AGN samples, including PG quasars and 2MASS red quasars (Shi et al. 2007). Whether this is separately true for those with and without hidden quasars (Ogle, Whysong, & Antonucci 2006) needs to be investigated. For only 4/17 radio MOHEGs do the spectra (Fig. 1) indicate a large star formation fraction (3C 31, 218, 293, and 315), with $L(\text{PAH}7.7)/L_{24} > 0.1$ (Fig. 12). Based on template fitting, the star formation contribution in 3C 31, 218 and 293 ranges from 87-100% at 15 μm (Leipski et al. 2009). Using the same procedure, we find that 3C 315 has a 40-50% star formation contribution at 15 μm .

We use the observed 7.7 μm PAH luminosity to estimate star formation rates (SFRs, Table 13) for ra-

dio MOHEGs using the prescription of Roussel et al. (2001). We convert the 11.3 μm PAH luminosity to 7.7 μm PAH luminosity, dividing by the mean 11.3/7.7 μm PAH ratio of 0.26 (Smith et al. 2007) to make an equivalent SFR estimate for sources where the 7.7 μm PAH is not detected. Note that the SFRs are integrated over the *Spitzer* IRS slit, which does not cover the whole galaxy for most of the observations (Figs. 1-4). The SFRs for MOHEGs with detected 7.7 μm PAH emission range from $4 \times 10^{-3} M_{\odot} \text{ yr}^{-1}$ for 3C 272.1 at the low end to $2.6 M_{\odot} \text{ yr}^{-1}$ for 3C 436 on the high end. Since the 11.3/7.7 μm PAH ratio is systematically enhanced compared to normal star-forming galaxies (Fig. 13), the 11.3 μm PAH star-formation rates should be considered upper limits and used with caution.

11. AGN ACTIVITY

Most (13/17) of the radio MOHEGs are mid-IR weak¹ (Ogle, Whysong, & Antonucci 2006; Leipski et al. 2009), with $\nu L_{\nu}(24\mu\text{m}) < 2 \times 10^{10} L_{\odot}$ (Table 9). Most are also optically classified as low-ionization galaxies (LIGs, Table 1) based on their low [OIII] 5007/[OII] 3727 ratios. Using the optical emission line measurements of Buttiglione et al. (2009), we construct BPT diagnostic diagrams (Baldwin et al. 1981), which show that most radio MOHEGs are LINERs according to the Kewley et al. (2006) line ratio criteria (Fig. 15). We can not say whether this tendency of radio MOHEGs to host MIR-weak, LINER AGNs is intrinsic or rather represents a bias against detecting low-equivalent width H₂ emission lines and PAH features against the stronger continuum in the MIR-luminous HIGs and BLRGs.

The mid-IR forbidden line ratios of radio MOHEG LINERs (Fig. 16) are similar to those of other LINERs observed by *Spitzer*, with [Ne III]/[Ne II] < 2.0, [O IV]/[Ne II] < 1.0, [S III]/[Ne II] < 1.0, and [S III]/[Si II] < 0.5 (Sturm et al. 2006; Dale et al. 2006; Dudik et al. 2009). The low [S III]/[Si II] ratio in particular is characteristic of AGN X-ray dissociation regions (Dale et al. 2006), in contrast to the higher ratio typical of star-forming galaxies. The [Ne III]/[Ne II] and [S III]/[Si II] ratios of radio MOHEGs are however considerably greater than what are seen in the Stephan’s Quintet main shock (Cluver et al. 2010). This may indicate that radio MOHEG forbidden line emission is associated primarily with the AGN rather than the shocked H₂ emission region. On the other hand, we can not rule out the possibility of a significant contribution from fast J-type shocks (with similar line ratios to LINERs) to the optical and MIR forbidden emission lines, (e.g., 3C 326, Nesvadba et al. 2010).

The three radio MOHEGs with Seyfert-like, high-ionization optical spectra (Cyg A, 3C 433, and 436) all have [Ne III]/[Ne II] > 2.0 and [O IV]/[Ne II] > 2.0. High ionization [Ne V] and [Ne VI] lines are detected in Cyg A and 3C 433, but only the [Ne VI] 7.65 μm line is detected in 3C 436 (Table 8). All three host powerful, hidden quasars with $\nu L_{\nu}(24\mu\text{m}) > 2 \times 10^{10} L_{\odot}$, and deep silicate troughs ($\tau_{9.7} > 0.5$) in-

¹ The wavelength used in the Ogle, Whysong, & Antonucci (2006) definition of MIR-weak ($\nu L_{\nu}(15\mu\text{m}) < 8 \times 10^{43} \text{ erg s}^{-1} = 2 \times 10^{10} L_{\odot}$) is different than the one we employ here, because of the need to accommodate a different redshift range.

dicating obscuration of the AGN by additional cold dust (Ogle, Whysong, & Antonucci 2006). Polarized, scattered broad emission lines are seen in the optical spectra of Cyg A (Ogle et al. 1997) and 3C 433 (Ogle et al., in preparation), confirming the presence of hidden quasar nuclei. The [Ne v] and [Ne vi] lines are detected at 2-3 σ in Cen A (see also Weedman et al. 2005; Mirabel et al. 1999), which may contain a hidden Seyfert nucleus (Whysong & Antonucci 2004; Leipski et al. 2009).

12. INSUFFICIENCY OF AGN X-RAY HEATING AS AN H₂ POWER SOURCE

The lack of a high-luminosity, high-ionization AGN in most radio MOHEGs indicates weak accretion onto the central supermassive black hole. Such low luminosity AGNs are insufficient to power the H₂ emission via X-rays.

The process of H₂ heating by X-rays in X-ray dissociation regions (XDRs) is described by Maloney et al. (1996). In their XDR models, 30-40% of the absorbed X-ray flux goes into gas heating via photoelectrons. The atomic photoelectric cross section energy dependence is $E^{-8/3}$, so that photoionizations in the energy range 1-30 keV are important. For a standard AGN X-ray power law spectrum with frequency dependence $\nu^{-0.7}$, $L(1-30\text{keV})/L(2-10\text{keV}) = 2.3$.

For a characteristic observed H₂ temperature of 200 K (corresponding to an ionization parameter $\log \xi_{\text{eff}} = -2.6$) the cooling by H₂ rotational lines in XDR models is $\sim 2\%$ of the total gas cooling (Maloney et al. 1996, Figs. 3a,5). At this temperature, the ratio of the first four rotational lines to the total rotational line luminosity is $L(\text{H}_2 \text{ 0-0 S(0)-S(3)})/L(\text{H}_2) = 0.58$. Combining the above factors, we estimate a maximum H₂ to X-ray luminosity ratio of $L(\text{H}_2 \text{ 0-0 S(0)-S(3)})/L_X(2-10 \text{ keV}) < 0.01$. This ratio is conservative, since it assumes that all of the X-ray flux from the AGN is absorbed by the XDR.

We compare unabsorbed nuclear X-ray (2-10 keV) luminosities measured by *Chandra* (Table 9) with the summed H₂ S(0)-S(3) line luminosities measured by *Spitzer* (Fig. 17). Two sources lack X-ray nuclear flux measurements (3C 310 and 424). We find $L(\text{H}_2)/L_X(2-10 \text{ keV}) > 0.01$ in all measured radio MOHEGs and SINGS AGNs, except Cyg A. The warm H₂ in Cyg A would have to intercept and absorb $> 30\%$ of the X-ray luminosity from the AGN to produce the observed mid-IR H₂ line luminosity. For all other sources, the observed rotational $L(\text{H}_2)/L_X(2-10 \text{ keV})$ exceeds the maximum XDR H₂ to X-ray luminosity ratio estimated above. The large scatter (nearly 5 dex) in the observed ratio $L(\text{H}_2)/L_X(2-10 \text{ keV}) = 0.002 - 100$ also argues strongly against X-ray heating as the primary driver of H₂ emission in radio galaxies or SINGS AGNs.

13. HOST GALAXIES AND ENVIRONS

Many radio MOHEGs (Table 3 and Figs. 1-4) appear to have a galactic stellar disk (Donzelli et al. 2007), dust disk, or dust lanes (De Koff et al. 2000). Stellar or dust disks may indicate a past gas-rich merger, which would help to explain the presence of large quantities of H₂. Most of the other galaxies are peculiar or distorted in their stellar isophotes. Only 3C 386 appears to have a regular elliptical host morphology.

There is evidence for patchy or organized dust absorp-

tion in 12/17 radio MOHEGs (Table 3). This is important because H₂ forms most easily in the presence of dust. Dust masses measured from HST optical images (De Koff et al. 2000) are typically $< 1\%$ of the warm H₂ mass measured with *Spitzer* (Table 12). However, this method likely underestimates the total dust mass associated with the warm H₂ and cold CO. The hosts of 3C 31 and 270 have striking dust disks and Cen A has thick dust lanes from an edge-on warped disk. Dust lanes, patchy dust, or dust filaments are also seen in Per A, 3C 272.1, 293, 315, 317, 338, Cyg A, 3C 433, and 436. The only galaxies without obvious dust absorption are Hydra A, 3C 310, 326 N, 386, and 424. However, dust absorption could be missed in the HST snapshots because of a smooth dust distribution or low galaxy inclination.

Interestingly, 14/17 radio MOHEGs belong to close galaxy pairs, groups or clusters (Table 3). Of these, 3 reside in pairs, 3 in groups, 1 in a poor X-ray detected cluster, and 7 in X-ray luminous clusters. Four of the clusters (hosting Per A, Hydra A, 3C 317, and 3C 338) are so-called cool-core clusters with ~ 3 keV gas temperatures and high central X-ray surface brightness. The cooling flow phenomenon may be a way to deliver large quantities of gas to these radio MOHEGs. FR I radio galaxies tend to reside in rich environments at low redshift (Longair & Seldner 1979; Heckman et al. 1985), while low- z FR II radio galaxies prefer the field. Because radio MOHEGs are found in both environments, cluster membership is apparently not a prerequisite for the H₂ emission phenomenon. Gravitational interactions with nearby companions may play a significant role in delivering or driving the molecular gas into the center of radio MOHEGs in the field or in clusters. A statistical comparison of the frequency of physical galaxy pairs in the H₂ detected and nondetected radio galaxy subsamples is outside the scope of this paper.

There are tidal distortions indicating strong interactions in at least 4/7 galaxy pairs, groups, and poor clusters: 3C 293, 310, 326, and 433. The 3C 31 and 3C 315 pairs do not show strong distortion, but the halos of close companions appear to overlap the primary galaxy. The Virgo cluster galaxy 3C 270 (NGC 4261) has a faint tidal tail (Tal et al. 2009). The 4 cool-core cluster cDs and 3C 433 have large, diffuse halos which appear to envelop two or more galaxies in the cluster centers. The three galaxies that do not reside in pairs, groups or clusters are 3C 386, 436, and Cen A. The warped, dusty molecular disk in Cen A may be the result of an elliptical/spiral merger (Baade & Minkowski 1954; Quillen et al. 2006). The host of 3C 436 shows signs of a recent merger, including a second nucleus and other irregularities in its surface brightness (McLure et al. 1999). The Virgo cluster galaxy 3C 272.1 (M84), the group galaxy 3C 424, and the isolated galaxy 3C 386 show no obvious signs of recent interaction.

14. RADIO SOURCE MORPHOLOGIES

The radio MOHEGs in our sample cover a large range of radio luminosity $\nu L_\nu(178\text{MHz}) = 10^{39} - 10^{44} \text{ erg s}^{-1}$ (Table 9 and Fig. 18). They display a motley collection of radio morphologies (Tables 1 and 2). There are 6 FR IIs and 11 FR Is. The fraction of FR II MOHEGs is comparable to the fraction of FR I MOHEGs in the

sample ($22 \pm 9\%$ vs. $39 \pm 12\%$). However, there could potentially be a bias against detecting H_2 in FR IIs with hidden quasars because the emission lines might be overwhelmed by copious warm dust emission.

Further classification of radio morphologies is somewhat subjective but may offer clues to the origin of radio MOHEGs. Looking at their morphology subclassifications (Table 1), 5/11 FR Is are classical twin jet (TJ) sources, 4/11 are fat doubles (FD), 1/11 is a double-double (DD), and 1/11 has a compact symmetric core (CSC). Of the FR IIs, only 3/6 are classical doubles, 1/6 is a fat double (FD), and 2/6 are X-shaped (X). There is a relatively large fraction of distorted radio sources compared to the rest of the sample, which only has 2/38 FD and 0/38 X-shaped sources. The two X-shaped radio sources (3C 433 and 3C 315) and the very peculiar source 3C 338 may be distorted by the motions of their interacting hosts or have jets deflected by their companions.

The radio MOHEGs also include a high fraction (3/17) of so-called restarting double-double (DD) or CSC sources, compared to 1/38 of the H_2 nondetected radio galaxies. The radio map of 3C 424 shows a brighter inner set of lobes surrounded by a fainter set of lobes that appears to originate from a previous spurt of activity (Black et al. 1992). High resolution maps of 3C 293 and 315 reveal bright, inner, compact symmetric double radio lobes roughly aligned with the larger scale radio lobes. These may represent new outbursts of radio activity or interaction of the small scale radio source with the host galaxy ISM. The radio cores also appear relatively bright in 3C 310, and 386, perhaps also indicating rejuvenated jets, or else high Doppler beaming factor. The restarting jet phenomenon may be connected to a new supply of fuel provided by the large mass of H_2 in these galaxies. Interaction between the restarting jet and the host galaxy ISM may play an important role in heating the H_2 .

15. DISCUSSION

15.1. Radio-Jet Feedback

The high incidence of MOHEGs in our radio-selected sample may indicate that the radio jets or lobes power the H_2 emission. However, there is at best a weak correlation between radio MOHEG H_2 luminosity and 178 MHz radio lobe power L_{178} (Fig. 18a). The linear Pearson correlation coefficient is $R = 0.79$, which reduces to $R = 0.35$ ($< 17\%$ probability of a chance correlation) when removing the partial correlation of luminosity with distance. For MOHEGs, there is a large range $L(\text{H}_2)/L_{178} = 0.004 - 6$ in the ratio of H_2 luminosity to low-frequency radio lobe synchrotron luminosity. The upper limits for H_2 nondetected radio galaxies have similar scatter, with a lower median ratio than the radio MOHEGs in this plot. The available mass of H_2 must be a limiting factor, and is likely an important source of scatter in the H_2 luminosity.

Scatter in the 178 MHz radio luminosity may be caused by environmental density variations or spectral aging of the radio lobes. Size and time scale differences between the radio and H_2 emission regions may also be important. For most sources, the spatially unresolved (kpc scale) H_2 emission region is much smaller than the ra-

dio source, which extends far beyond the host galaxy (50 kpc-1 Mpc). The extended radio emission may not give a reliable indicator of the jet power dissipated at kpc scale. However, while the H_2 cooling time scale is only $\sim 10^4$ yr, the dissipation timescale of the molecular gas kinetic energy may be even greater than the typical radio source lifetime of $\sim 10^7$ yr (Nesvadba et al. 2010). Therefore, variations in jet power over the lifetime of the radio jet may not cause significant variations in the H_2 luminosity.

There is no significant correlation between $L(\text{H}_2)$ and the 5 GHz radio core power L_5 measured at arsecond scales (Fig. 18b). This is not surprising since relativistic beaming can boost or de-boost the core flux by a large factor. Differences in radio spectral shape may also be large at this high frequency. Neither is there a correlation of $L(\text{H}_2)/L(\text{PAH7.7})$ with L_{178} nor L_5 (Fig. 18c,d). This ratio and the fraction of warm/cold H_2 may depend on a number of factors, including the spatial distribution of H_2 relative to the radio source, the pressure of the hot ISM, and the detailed jet-ISM interaction history.

It is instructive to compare radio MOHEGs to dusty elliptical MOHEGs selected by IRAS (Kaneda et al. 2008). We estimate 178 MHz luminosities for 12 ellipticals by interpolating or extrapolating $100 - 10^3$ MHz radio fluxes measured by the NVSS, SUMSS, or FIRST surveys, or fluxes available in NED (Fig. 18a, c). These galaxies are up to 100 times fainter than radio MOHEGs at 178 MHz, and extend the MOHEG $L(\text{H}_2)$ vs. L_{178} parameter space. The faintest radio sources with $L_{178} < 10^{38}$ erg s $^{-1}$ (in NGC 2974, NGC 3894, IC 3370, and NGC 5044) lie well above the $L(\text{H}_2)$ vs L_{178} locus established by radio MOHEGs, with $L(\text{H}_2)/L_{178} > 50$. We suggest that these weak radio sources may be radio galaxies that are currently in between strong radio jet outbursts. This hypothesis can be tested by searching for low-frequency radio relics. The H_2 emission may be powered by residual kinetic energy injected into the ISM by previous radio jet activity. The H_2 luminosity floor of $L(\text{H}_2) \sim 10^{39}$ erg s $^{-1}$ may be set by the ratio of the H_2 kinetic energy dissipation timescale and the mean time between radio outbursts. Alternatively, this low level of H_2 emission could be powered by gas accretion or X-ray emission from a weak AGN. It will be important to test the latter possibility with additional *Chandra* observations.

Several of the radio MOHEGs that reside in X-ray bright clusters show evidence that the radio lobes have displaced the intracluster medium (ICM) in X-ray cavities. For these sources, it is possible to estimate the $4pV$ energy required to excavate the cavities, and divide by the buoyancy time scale to estimate the average jet power deposited into the ICM (Rafferty et al. 2006). These jet cavity powers fall in the range $10^{42} - 10^{45}$ erg s $^{-1}$ and the ratio of H_2 luminosity to jet cavity power falls in the range $1 \times 10^{-4} - 3 \times 10^{-3}$ (Table 14). This demonstrates that the jet power is more than sufficient to produce the observed H_2 luminosity, modulo an unknown conversion efficiency.

One potential difficulty is efficiently coupling the jet power to the host galaxy ISM after the radio lobes have broken out of the host galaxy and are doing most of their work on the intergalactic medium. Ogle et al. (2007) argued that only 7×10^{-4} of the radio jet power in 3C 326

could be dissipated in the host galaxy ISM, based on the small ratio of radio core to Mpc-scale radio lobe flux. This in turn could only power $< 10\%$ of the observed H_2 luminosity, for an estimated jet kinetic luminosity of $\sim 10^{44} \text{ erg s}^{-1}$. Given the uncertainties in estimating jet kinetic luminosity and time variability, the inner radio jet could easily be ten times more powerful than this estimate. In addition, the radio core power is probably not a reliable tracer of jet kinetic power dissipation and may be strongly affected by Doppler boosting or de-boosting, as indicated by the large scatter in Figure 18b. Turning this problem around, the large H_2 luminosity from the center of 3C 326 N may indicate that a significant fraction of the radio jet power is dissipated inside the host galaxy, even though the radio lobes have long since escaped.

On the other hand, the compact symmetric radio lobes in the radio MOHEG 3C 293 (Evans et al. 1999; Emonts et al. 2005; Ogle et al. 2008; Papadopoulos et al. 2010) appear to be directly interacting with the host ISM. It will be important to measure the pressure in the hot interstellar medium with *Chandra* to determine if dissipation of jet kinetic energy can indeed power the H_2 emission in this and other kpc-size sources (e.g., 3C 315).

High-velocity neutral and ionized outflows have been observed in the radio MOHEG 3C 293, and there is morphological and kinematic evidence that these outflows are driven by the radio jet (Morganti et al. 2003; Emonts et al. 2005). Similar H I and ionized outflows have been found in several other low-redshift compact and extended radio sources (Morganti et al. 2005; Holt et al. 2008), with outflow speeds of up to 2000 km s^{-1} and mass-loss rates of up to $50 M_\odot \text{ yr}^{-1}$ indicating a strong interaction between the radio jet and the host galaxy ISM. Nesvadba et al. (2010) recently discovered a high velocity ($\sim 1000 \text{ km s}^{-1}$) neutral (Na I) outflow in 3C 326, the most extreme radio MOHEG. Even more spectacular jet driven ionized outflows, which may be responsible for ejecting a large fraction of the host galaxy ISM, are observed in high-redshift radio galaxies (Nesvadba et al. 2008).

The connection between jet driven outflows and H_2 emission in radio MOHEGs is studied in detail by Nesvadba et al. (2010). Since the molecular hydrogen must have high density and a low volume filling factor, it is likely that the cocoon of hot, shocked ISM surrounding the jet (Scheuer 1974; Begelman & Cioffi 1989) serves as an intermediary between the jet and the H_2 . The radio jet heats the diffuse ISM, which expands in a hot fast wind and drives shocks into ambient or entrained molecular clouds, powering the observed warm H_2 emission. For H_2 at densities of $10^3\text{-}10^4 \text{ cm}^{-3}$, the observed range of temperatures is characteristic of $5\text{-}20 \text{ km s}^{-1}$ shock velocities (Guillard et al. 2009).

The relative velocity and shear between the molecular clouds and hot wind may ultimately power the H_2 emission through turbulent mixing layers (Nesvadba et al. 2010; Guillard et al. 2009). The hydrodynamical stability of the H_2 emitting clouds needs to be investigated, as they may be ablated by the hot wind and may eventually dissolve completely. However, there is evidence that the atomic and H_2 filaments in Per A are held together by

strong magnetic fields (Fabian et al. 2008). Moreover, the fact that H_2 is the primary coolant only in magnetic (C-type) shocks strongly suggests that the magnetic field plays an important role in MOHEGs.

15.2. Cosmic Ray Heating and Pressure

Another potentially important source of heating for warm H_2 in radio MOHEGs may be ionizing particles in the form of relativistic particles from the radio lobes. Ferland et al. (2008) have proposed cosmic rays or thermal particles from the surrounding hot gas as the dominant heat source powering the warm H_2 emission filaments in the Perseus A (3C 84) cool core cluster. An enhanced cosmic ray density has also been proposed to account for the high temperature of molecular clouds in the Milky Way nuclear disk (Yusef-Zadeh et al. 2007). We discuss this possibility for H_2 luminous radio galaxies.

The critical density of the S(0) and S(1) lines is sufficiently low (Le Bourlot et al. 1999; Wrathmall et al. 2007, $< 10^3 \text{ cm}^{-3}$ at $T > 100 \text{ K}$) that we can assume that the corresponding excited levels are thermalized by collisions. Thus, the line emission is cooling the gas and must be balanced by gas heating. In our radio MOHEG sample, the mean of total line emission per warm H_2 molecule (in the lowest temperature component, Table 11) is observed to be $7 \times 10^{-24} \text{ erg s}^{-1}$.

The molecular gas heating by cosmic rays is 4 eV per ionization in the MEUDON gas code (Le Petit et al. 2006). In CLOUDY, the heating efficiency increases with the gas ionization fraction; the heating per ionization is 7 eV for a ionization fraction of 10^{-4} characteristic of the diffuse interstellar medium where carbon is ionized (Shaw et al. 2005). The H_2 line cooling is balanced by cosmic ray heating for an ionization rate per hydrogen $\zeta \sim 7 \times 10^{-13} \text{ s}^{-1}$, a value 3.5×10^4 times higher than the standard Galactic rate (Shaw et al. 2005). For such a value, cosmic rays are the main destruction path of H_2 molecules and the molecular gas fraction depends on the ionization rate to gas density ratio ζ/n_H . Model calculations presented by Ferland et al. (2008) show that for $\zeta \sim 7 \times 10^{-13} \text{ s}^{-1}$ the gas is molecular for $n_H > 5 \times 10^4 \text{ cm}^{-3}$ (see their figure 2). Note that for such high densities H_2 rotational states are thermalized up to $J \geq 5$, and the higher J lines up to at least S(3) are also cooling lines.

Combining the lower limit on the gas density and the warm H_2 temperature ($\sim 200 \text{ K}$) inferred from the S(1) to S(0) line ratio we get a warm molecular gas pressure $\sim 10^7 \text{ K cm}^{-3}$ which is a factor 1400 higher than the mean cosmic ray pressure of $7.2 \times 10^3 \text{ K cm}^{-3}$ in the Milky Way disk (Boulares & Cox 1990). For a cosmic ray energy density 3.5×10^4 times the Galactic mean value, the cosmic ray pressure would be 25 times larger than the thermal gas pressure (assuming that the cosmic ray pressure scales linearly with the ionization rate). Such a large difference in pressure would seem unsustainable, however it could in principle be supported by magnetic pressure in the compressed magnetic field within molecular clouds (Pellegrini et al. 2009). Therefore, heating by cosmic rays from the radio lobes or hot gas in the radio jet cocoon may present an alternative or additional pathway to heat H_2 by radio-jet feedback.

15.3. Gas Supply from Cooling Flows and Galaxy Collisions

An important unanswered question is the origin of large quantities of molecular gas in radio MOHEGs. Copious amounts ($10^9 - 10^{11} M_{\odot}$) of cold molecular gas discovered in $\sim 45\%$ of BCGs in X-ray selected cool-core clusters (Edge 2001; Salome & Combes 2003) may be deposited by cooling flows. H_2 emission from warm molecular gas also appears to be common in cool-core BCGs (Egami et al. 2006; Johnstone et al. 2007; De Messieres et al. 2009). Since a large fraction of these BCGs host radio sources, the H_2 emission could potentially be excited by radio jet feedback. The gas cooling rates in the radio MOHEGs that reside in cool core clusters are $10 - 200 M_{\odot} \text{ yr}^{-1}$ (Peterson et al. 2003; Hicks & Mushotzky 2005), enough to supply the observed molecular gas masses in < 1 Gyr.

Gas-rich galaxy collisions or tidal interactions with nearby galaxies may drive gas into the center of radio galaxies in less rich environments (Ogle et al. 2007). This is an attractive possibility, considering that most radio MOHEGs are mergers or have nearby companions, and several display prominent tidal distortions. In comparison, most field elliptical galaxies and 3C radio galaxies in the nearby universe are poor in molecular gas ($< 10^9 M_{\odot}$, Combes et al. 2007; Lim et al. 2003; Ocana Flacquer et al. 2010). Galaxy collision driven inflows and jet induced outflows may constitute another, intermittent type of AGN feedback loop (e.g., Appleton et al. 2002).

While cooling flows or galaxy collisions may deliver the molecular gas in radio MOHEGs, it seems unlikely that gas accretion or galaxy collisions contribute significantly to heating the H_2 . Unlike the galaxy-collision powered H_2 emission from Stephan's Quintet (Appleton et al. 2006), the bulk of the H_2 emission is concentrated inside the central ~ 10 kpc of radio galaxies. We are pursuing higher resolution spectroscopy of mid-IR and near IR H_2 emission lines in order to determine the dynamical state of the warm molecular gas.

16. CONCLUSIONS

(1.) We detect high luminosity H_2 emission lines from 17/55 (31% of) radio galaxies at $z < 0.22$ observed with *Spitzer* IRS at low resolution.

(2.) We redefine molecular hydrogen emission galaxies (MOHEGs) to be galaxies with $L(H_2)/L(\text{PAH}7.7) > 0.04$. This puts 16/17 of the H_2 -detected radio galaxies (radio MOHEGs) in this rapidly growing, new class of

galaxies.

(3.) Large H_2/PAH ratios indicate that the H_2 emission from MOHEGs is most likely powered by shocks. We can not completely rule out a contribution from cosmic ray heating, though it would require cosmic ray pressures that exceed the gas pressure by a large factor.

(4.) The star formation rates in radio MOHEGs range from very low to moderate ($4 \times 10^{-3} - 3 M_{\odot} \text{ yr}^{-1}$), and the $24 \mu\text{m}$ continuum is dominated by the AGN in 13/17 of these galaxies.

(5.) Most MOHEG AGNs in our sample are mid-IR weak and have low-ionization forbidden emission line spectra.

(6.) AGN X-ray emission measured by *Chandra* is not luminous enough to power the H_2 emission in MOHEGs.

(7.) All but one of the radio MOHEGs in our sample reside in merger remnants, interacting pairs, groups, or clusters, supporting the hypothesis that galaxy interactions and mergers may deliver molecular gas or drive existing molecular gas into the central few kpc of radio galaxy hosts.

(8.) Radio jet driven outflows of hot gas may drive shocks into the molecular gas, powering the H_2 emission in radio MOHEGs. The jet power measured for radio MOHEGs in cool core clusters is more than sufficient to power the H_2 emission. Higher spatial resolution of the H_2 emission region and its kinematics will give further insights into the radio jet feedback mechanism.

This work is based primarily on observations made with the *Spitzer* Space Telescope, which is operated by the Jet Propulsion Laboratory, California Institute of Technology under NASA contract 1407. Supporting observations were retrieved from the *Chandra* archive, maintained by the Chandra X-ray Observatory Center, which is operated by the Smithsonian Astrophysical Observatory on behalf of NASA. Optical *Hubble* images and NUV GALEX data were retrieved via MAST, operated by the Space Telescope Science Institute for NASA. We have made use of the NASA/IPAC Extragalactic Database (NED) which is operated by the Jet Propulsion Laboratory, California Institute of Technology, under contract with NASA. Support for this research was provided by NASA through an award issued by JPL/Caltech. We thank Bill Reach for providing us with his H_2 fitting code. We also thank Simona Giacintucci for providing the low frequency radio flux of the MOHEG elliptical NGC 5044 in advance of publication.

REFERENCES

- Appleton, P. N. et al. 2006, ApJ, 639, L51
 Appleton, P.N., Charmandaris, V., Gao, Y., Combes, F. Ghigo, F., Horrelou, C., & Mirabel, I.F. 2002, ApJ, 566, 682
 Armus, L. et al. 2006, ApJ, 640, 204
 Baade, W., & Minkowski, R. 1954, ApJ, 119, 215
 Baars, J. W. M., Genzel, R., Pauliny-Toth, I. I. K., & Witzel, A. 1977, A&A, 61, 99
 Bakes, E. L. O., Tielens, A. G. G. M., & Bauschlicher, C. W. 2001, ApJ, 556, 501
 Baldwin, J. A., Phillips, M. M., & Terlevich, R. 1981, PASP, 93, 5
 Balmaverde, B., Capetti, A., & Grandi, P. 2006, A&A, 451, 35
 Begelman, M. C. & Cioffi, D. F. 1989, ApJ, 345, L21
 Black, A. R. S., Baum, S. A., Leahy, J. P., Perley, R. A., Riley, J. M., & Scheuer, P. A. G. 1992, MNRAS, 256, 186
 Boulares, A. & Cox, D. P. 1990, ApJ, 365, 544
 Burbidge, E. M. & Burbidge, G. R. 1965, ApJ, 142, 1351
 Buttiglione, S. et al. 2009, A&A, 495, 1033
 Cesarsky, D., Cox, P., Pineau des Forets, G., van Dishoeck, E. F., Boulanger, F., & Wright, C. M. 1999, A&A, 348, 945
 Chiar, J. E., & Tielens, A. G. G. M. 2006, ApJ, 637, 774
 Churazov, E., Forman, W., Jones, C., & Bohringer, H. 2000, A&A, 356, 788
 Ciotti, L. & Ostriker, J. P. 2007, ApJ, 665, 1038
 Cleary, K., Lawrence, C. R., Marshall, J. A., Hao, L., & Meier, D. 2007, ApJ, 660, 117
 Cluver, M. E., Appleton, P. N., Guillard, P., Boulanger, F., Ogle, P., Duc, P.-A., Lu, N., Rasmussen, J., Reach, W. T., Smith, J. D., Tuffs, R., Xu, K., Yun, M. 2010, ApJ, 710, 248

- Combes, F., Young, L. M., & Bureau, M. 2007, *MNRAS*, 377, 1795
- Cowie, L. L., Hu, E. M., Jenkins, E. B., & York, D. G. 1983, *ApJ*, 272, 29
- Conselice, C. J., Gallagher, J. S., & Wyse, R. F. G. 2001, *AJ*, 122, 2281
- Crawford, C. S., Allen, S. W., Ebeling, H., Edge, A. C., & Fabian, A. C. 1999, *MNRAS*, 306, 857
- Croton, D. J. et al. 2006, *MNRAS*, 365, 11
- Dale et al. 2006, *ApJ*, 646, 161
- Desai et al. 2007, *ApJ*, 669, 810
- De Koff, S., Best, P., Baum, S. A., Sparks, W., Rottgering, H., Miley, G., Golombek, D., Macchetto, F., & Martel, A. 2000, *ApJS*, 129, 33
- De Messieres, G. E., O'Connell, R. W., McNamara, B. R., Donahue, M., Nulsen, P. E. J., Voit, G. M., & Wise, M. W. 2009, *ASPCS*, in press, arXiv:0908.3445
- Donahue, M., Mack, J., Voit, G. M., Sparks, W., Elston, R., & Maloney, P. R. 2000, *ApJ*, 545, 670
- Donzelli, C. J., Chiaberge, M., Macchetto, F. D., Madrid, J. P., Capetti, A., & Marchesini, D. 2007, *ApJ*, 667, 780
- Dopita, M. A. & Sutherland, R. S. 1996, *ApJS*, 102, 161
- Draine, B. T. & Li, A. 2001, *ApJ*, 551, 807
- Dudik, R. P. Satyapal, S., & Marcu, D. 2009, *ApJ*, 691, 1501
- Edge, A. C. 2001, *MNRAS*, 328, 762
- Egami, E., Rieke, G. H., Fadda, D., & Hines, D. C. 2006, *ApJ*, 652, L21
- Emonts, B. H. C., Morganti, R., Tadhunter, C. N., Oosterloo, T. A., Holt, J., & van der Hulst, J. M. 2005, *MNRAS*, 362, 931
- Evans, D. A., Worrall, D. M., Hardcastle, M. J., Kraft, R. P., & Birkinshaw, M. 2006, *ApJ*, 642, 96
- Evans, A. S., Mazzarella, J. M., Surace, J. A., Frayer, D. T., Iwasawa, K., & Sanders, D. B. 2005, *ApJS*, 159, 197
- Evans, A. S., Sanders, D. B., Surace, J. A., & Mazzarella, J. M. 1999, *ApJ*, 511, 730
- Fabian, A. C., Johnstone, R. M., Sanders, J. S., Conselice, C. J., Crawford, C. S., Gallagher, J. S. III, & Zweibel, E. 2008, *Nature*, 454, 968
- Fanaroff, B. L. & Riley, J. M. 1974, *MNRAS*, 167, 31
- Ferland, G. J., Fabian, A. C., Hatch, N. A., Johnstone, R. M., Porter, R. L., van Hoof, P. A. M., & Williams, R. J. R. 2009, *MNRAS*, 392, 1475
- Ferland, G. J., Fabian, A. C., Hatch, N. A., Johnstone, R. M., Porter, R. L., van Hoof, P. A. M., & Williams, R. J. R. 2008, *MNRAS*, 386, L72
- Flagey, N., Boulanger, F., Verstraete, L., Miville Deschenes, M. A., Noriega Crespo, A. & Reach, W. T. 2006, *A&A*, 453, 969
- Goudfrooij, P. & de Jong, T. 1995, *A&A*, 298, 784
- Gracia-Carpio J., Planesas, P., & Colina, L. 2007, *A&A*, 468, L67
- Granato, G., De Zotti, G., Silva, S., Bressan, A., & Danese, L. 2004, *ApJ*, 600, 580
- Guillard, P., Boulanger, F., Cluver, M., Appleton, P. N., Pineau des Forets, G., & Ogle, P. 2010, *A&A*, submitted
- Guillard, P., Boulanger, F., Pineau des Forets, G., & Appleton, P. N. 2009a, *A&A*, 502, 515
- Habing, H. J. 1968, *BAN*, 19, 421
- Haas, M., Willner, S. P., Heymann, F., Ashby, M. L. N., Fazio, G. G., Wilkes, B. J., Chini, R., & Siebenmorgen, R. 2008, *ApJ*, 688, 122
- Hardcastle, M. J., Evans, D. A., & Croston, J. H. 2006, *MNRAS*, 370, 1893
- Hatch, N. A., Crawford, C. S., Johnstone, R. M., & Fabian A. C. 2005, *MNRAS*, 358, 765
- Heckman, T. M., Baum, S. A., van Breugel, W. J. M., & McCarthy, P. 1989, *ApJ*, 338, 48
- Heckman, T. M., Carty, T. J., & Bothun, 1985, *ApJ*, 288, 122
- Heckman, T. M. 1981, *ApJ*, 250, L59
- Hicks, A. L., & Mushotzky, R. 2005, *ApJ*, 635, L9
- Higdon, S. J. U., Armus, L., Higdon, J. L., Soifer, B. T., & Spoon, H. W. W., 2006, *ApJ*, 648, 323
- Holt, J., Tadhunter, C. N., & Morganti, R. 2008, *MNRAS*, 387, 639
- Hopkins, P. F., Hernquist, L., Cox, T. J., Di Matteo, T., Robertson, B., & Springel, V. 2006, *ApJS*, 163, 1
- Houck, J. R. et al. *ApJS*, 154, 18
- Israel, F. P., van Dishoeck, E. F., Baas, F., Koornneef, J., Black, J. H., de Graauw, T. 1990, *A&A*, 227, 342
- Joseph, R. D. & Wright, G. S. 1984, *Nature*, 311, 132
- Johnstone, R. M., Hatch, N. A., Ferland, G. G., Fabian, A. C., Crawford, C. S., & Wilman, R. J. 2007, *MNRAS*, 382, 1246
- Johnstone, R. M., Fabian, A. C., & Nulsen, R. J. 1987, *MNRAS*, 224, 75
- Kaneda, H., Onaka, T., Sakon, I., Kitayama, T., Okada, Y., & Suzuki, T. 2008, *ApJ*, 684, 270
- Kellermann, K. I., Pauliny-Toth, I. I. K., & Williams, P. J. S. *ApJ*, 157, 1
- Kenney, J. D. P., Tal, T., Crowl, H. H., Feldemeir, J., & Jacoby, G. H. *ApJ*, 687, L69
- Kent, S. M. & Sargent, W. L. W. 1979, *ApJ*, 230, 667
- Kewley, L. J., Groves, B., Kauffmann, G., & Heckman, T. 2006, *MNRAS*, 372, 961
- Komossa, S., Burwitz, V., Hasinger, G., Predehl, P., Kaastra, J. S., & Ikebe, Y. 2003, *ApJ*, 582, L15
- Kuhr, H., Witzel, A., Pauliny-Toth, I. I. K., & Nauber, U. 1981, *A&AS*, 45, 367
- Laing, R. A., Riley, J. M., & Longair, M. S. 1983, *MNRAS*, 204, 151
- Le Bourlot, J., Pineau des Forets, G., & Flower, D. R. 1999, *MNRAS*, 305, 802
- Le Petit, F., Nehme, C., Le Bourlot, J., & Roueff, E. 2006, *ApJS*, 164, 506
- Leipski, C., Antonucci, R., Ogle, P., & Whysong, D. 2009, *ApJ*, 701, 891
- Lim, J., Leon, S., Combes, F., & Trung, D.-V., 2003, *ASPC*, 290, 529
- Longair, M. S., & Seldner, M. 1979, *MNRAS*, 189, 433
- Lutz, D., Sturm, E., Genzel, R., Spoon, H. W. W., Moorwood, A. F. M., Netzer, H., & Sternberg A. 2003, *A&A*, 409, 867
- Lynds, R. 1970, *ApJ*, 159, L151
- McNamara, B. R. et al. 2000, *ApJ*, 534, L135
- Maloney, P. R., Hollenbach, D. J., & Tielens, A. G. G. M. 1996, *ApJ*, 466, 561
- Max, C., Canalizo, G., Macintosh, B. A., Raschke, L., Whysong, D., Antonucci, R., & Schneider, G. 2005, *ApJ*, 621, 738
- McLure, R. J., Kukula, M. J., Dunlop, J. S., Baum, S. A., O'Dea, C. P., & Hughes, D. H. 1999, *MNRAS*, 308, 377
- Merloni, A., & Heinz, S. 2008, *MNRAS*, 388, 1011
- Micelotta, E. R., Jones, A. P., Tielens, A. G. G. M. 2010a, *A&A*, 510, A36
- Micelotta, E. R., Jones, A. P., Tielens, A. G. G. M. 2010b, *A&A*, 510, A37
- Minkowski, R. 1957, in *IAU Symposium 4, Radio Astronomy*, ed. H. C. van de Hulst (Cambridge: Cambridge University Press), p. 107.
- Mirabel, I. F. et al. 1999, *A&A*, 341, 667
- Morganti, R., Tadhunter, C. N., & Oosterloo, T. A. 2005, *A&A*, 444, L9
- Morganti, R., Oosterloo, T. A., Emonts, B. H. C., van der Hulst, J. M., & Tadhunter, C. N., 2003, *ApJ*, 593, L69
- Narron, R., Ogle, P., & Laher, R. R. 2007, *ASPC*, 376, 437, *ADASS XVI*, ed. R. Shaw, F. Hill, & D. Bell.
- Nesvadba, N. P. H., Boulanger, F., Salome, P., Guillard, P., Lehnert, M. D., Pineau des Forets, G., Ogle, P., & Appleton, P. 2010, *A&A*, in press
- Nesvadba, N. P. H., Lehnert, M. D., De Breuck, C., Gilbert, A. M., & van Breugel, W. 2008, *A&A*, 491, 407
- Neufeld, D. A., Hollenbach, D. J., Kaufman, M. J., Snell, R. L., Melnick, G. J., Bergin, E. A., & Paule, S. 2007, *ApJ*, 664, 890
- Neufeld, D. A. et al. 2006, *ApJ*, 649, 816
- Ocana Flaquer, B., Leon, S., Combes, F., & Lim, J. 2010, *A&A*, in press, arXiv:1001.5009
- Ogle, P., Antonucci, R., Leipski, C., Appleton, P., & Whysong, D. 2008, *ASPC*, 386, 15
- Ogle, P., Antonucci, R., Appleton, P. N., & Whysong, D. 2007, *ApJ*, 668, 699
- Ogle, P. M., Whysong, D. W., & Antonucci, R. 2006, *ApJ*, 647, 161
- Ogle, P. M., Cohen, M. H., Miller, J. S., Tran, H. D., Goodrich, R. W., & Fosbury, R. A. E. 1997, *ApJ*, 482, L37
- Okuda, T., Kohno, K., Iguchi, S., & Nakanishi, K. 2005, *ApJ*, 620, 673
- Papadopoulos, P. P., Van der Werf, P., Isaak, K., & Xilouris, E. M. 2010, *ApJ*, 715, 775
- Pellegrini, S. 2009, *ApJ*, 693, 285

- Pellegrini, S. 2005, MNRAS, 364, 169
- Peterson, J. R., Kahn, S. M., Paerels, F. B. S., Kaastra, J. S., Tamura, T., Bleeker, J. A. M., Ferrigno, C., & Jernigan, J. G. 2003, ApJ, 590, 207
- Phillips, T. G., Ellison, B. N., Keene, J. B., Leighton, R. B., Howard, R. J., Masson, C. R., Sanders, D. B., Veidt, B., & Young, K. 1987, ApJ, 322, L73
- Quillen, A. C., Brookes, M. H., Keene, J., Stern, D., Lawrence, C. R., & Werner, M. W. 2006, ApJ, 2006, 645, 1092
- Rafferty, D. A., McNamara, B. R., Nulsen, P. E. J., & Wise, M. W. 2006, ApJ, 652, 216
- Rapacioli, M., Joblin, C., & Boissel, P. 2005, A&A, 429, 193
- Rigopoulou, D., Kunze, D., Lutz, D., Genzel, R., & Moorwood, A. F. M. 2002, A&A, 389, 374
- Roussel, H. et al. 2007, ApJ, 669, 959
- Roussel, H., Sauvage, M., Vigroux, L., & Bosma, A. 2001, A&A, 372, 427
- Salome, P. et al. 2006, A&A, 454, 437
- Salome, P., & Combes, F. 2003, A&A, 412, 657
- Saripalli, L., & Mack, K.-H. 2007, MNRAS, 376, 1385
- Scannapieco, E. & Oh, S. P. 2004, ApJ, 608, 62
- Scheuer, P. A. G. 1974, MNRAS, 166, 513
- Schweitzer, M. et al. 2006, ApJ, 649, 79
- Shaw, G., Ferland, G. J., Abel, N. P., Stancil, P. C., & van Hoof, P. A. M. 2005, ApJ, 624, 794
- Shi, Y. et al. 2007, ApJ, 669, 841
- Sivanandam, S., Rieke, M. J., & Rieke, G. H. 2010, ApJ, in press, arXiv:0912.0075
- Smith, J. D., et al. 2007, ApJ, 656, 770
- Solomon, P. M. & Vanden Bout, P. A. 2005, ARAA, 43, 677
- Sturm, E. et al. 2006, ApJ, 653, L13
- Sutherland, R. S. & Bicknell, G. V. 2007, ApJS, 173
- Tadhunter, C., Dicken, D., Holt, J., Inskip, K., Morganti, R., Axon, D., Buchanan, C., Gonzalez Delgado, R., Barthel, P., & van Bemmel, I. 2007, ApJ, 661, L13
- Tal, T., Van Dokkum, P. G., Nelan, J., & Bezanson, R. 2009, AJ, 138, 1417
- Temi, P., Brighenti, F., & Matthews, W. G. 2007, ApJ, 660, 1215
- Tran, Q. D. et al. 2001, ApJ, 552, 527
- Ueda, Y., Ishisai, Y., Takahashi, T., Makishima, K., & Ohashi, T. 2005, ApJS, 161, 185
- Veilleux et al. 2009, ApJS, 182, 628
- Voit, M. 1991, ApJ, 379, 122
- Wilgenbus, D., Cabrit, S., Pineau des Forets, G., & Flower, D. R. 2000, A&A, 356, 1010
- Willett, K. W., Stocke, J. T., Darling, J., & Perlman, E. S. 2010, ApJ, in press, arXiv:1004.0952
- Wrathmall, S. A., Gusdorf, A., & Flower, D. R. 2007, MNRAS, 382, 133 [Wrt8907y]
- Yusef-Zadeh, F., Wardle, M., & Roy, S. 2007, ApJ 665, L123
- Weedman, D. W., Hao, L., Higdon, S. J. U., Devost, D., Wu, Y., Charmandaris, V., Brandl, B., Bass, E., & Houck, J. R. 2005, ApJ, 633, 706
- Whysong, D & Antonucci, R. 2004, ApJ, 602, 116
- Zakamska, N. 2010, Nature, 465, 60
- Zanni, C., Murante, G., Bodo, G., Massaglia, S., Rossi, P., & Ferrari, A. 2005, A&A, 429, 415

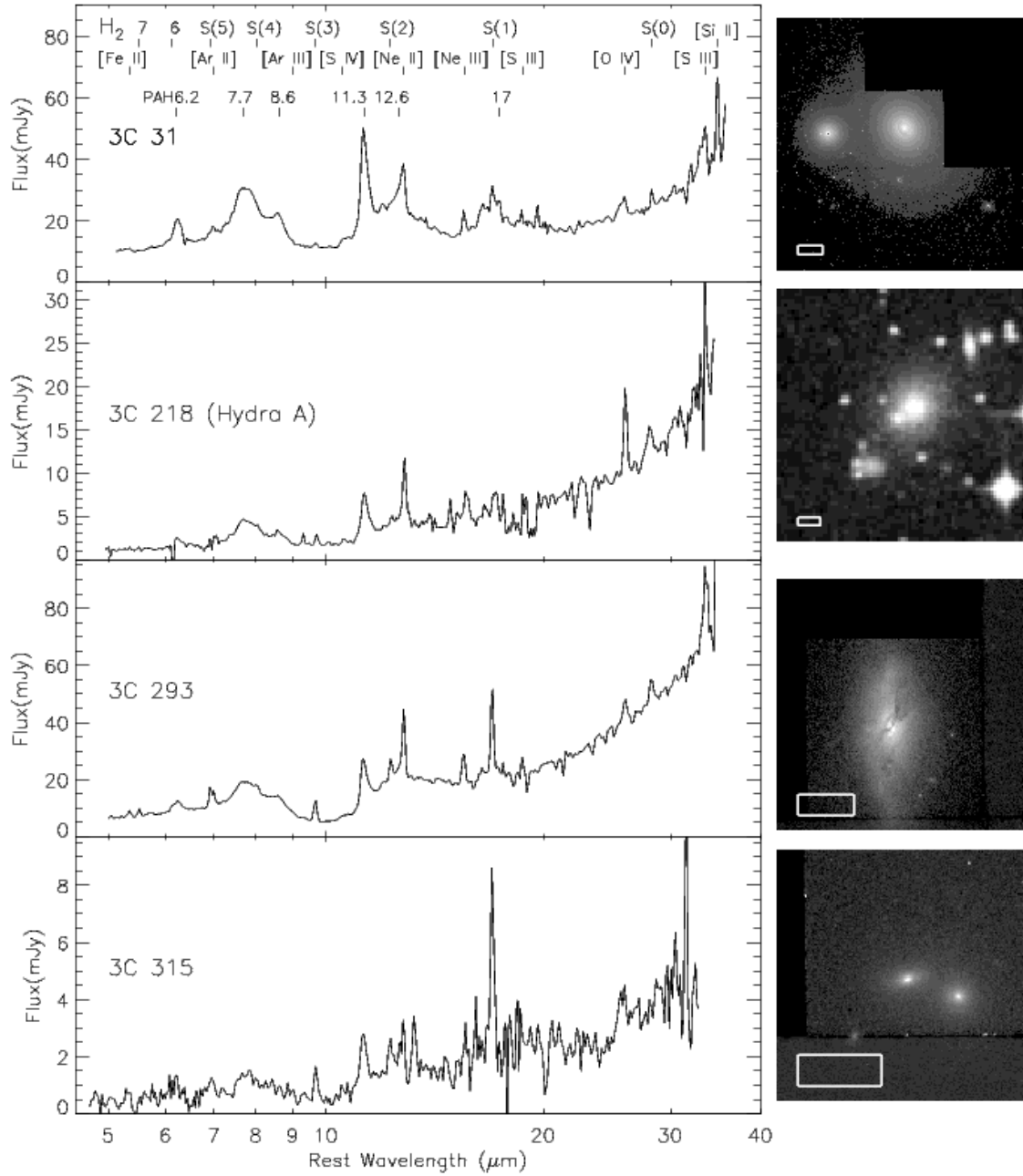


FIG. 1.— *Spitzer* IRS low-resolution spectra of 3C 31, 218 (= Hydra A), 293, and 315. These sources have strong PAH emission and 9.7 μm silicate absorption. Spectra are arranged in order of increasing equivalent width of the H_2 pure-rotational lines. Images to the right are from HST WFPC2 (3C 31, 293 and 315) and the UK Schmidt telescope (3C 218, from NED). The host of 3C 31 resides in the Arp 331 group. Hydra A resides in the cool core cluster A 780. The box at the lower left corner of each image shows the size of the $3''.7 \times 10''.0$ spectral extraction region at 10 μm .

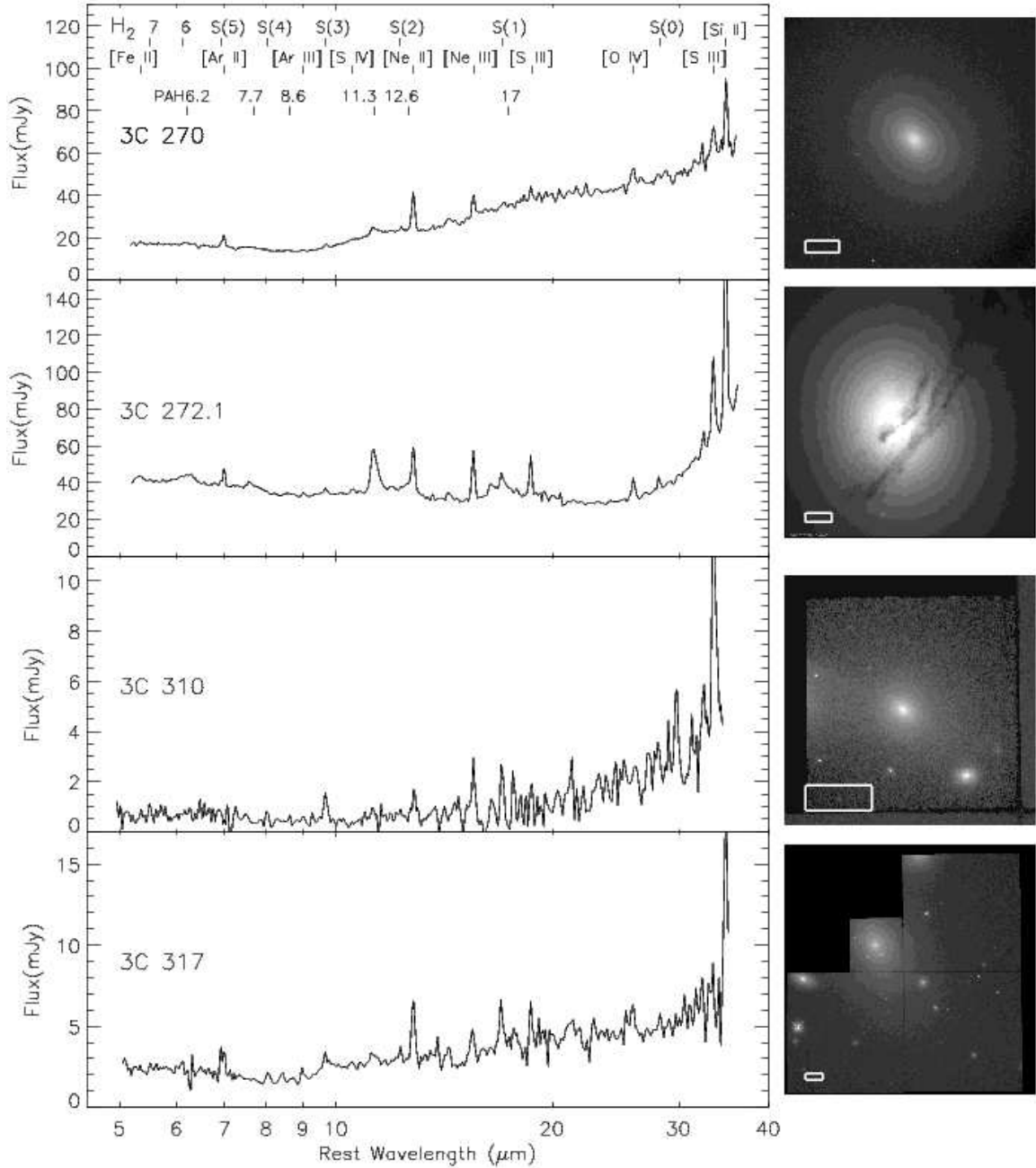


FIG. 2.— *Spitzer* IRS low-resolution spectra of 3C 270 (= NGC 4261), 3C 272.1 (= M 84), 3C 310, and 3C 317. These sources have weak $7.7\mu\text{m}$ PAH emission and weak-moderate $9.7\mu\text{m}$ silicate absorption. Note the extremely large PAH $11.3/\text{PAH } 7.7$ and PAH $17/\text{PAH } 7.7$ ratios and steeply rising continuum at $> 24\mu\text{m}$ in 3C 272.1. Radio galaxies 3C 270 and 272.1 reside in the Virgo Cluster, 3C 310 in a poor cluster, and 3C 317 in the A 2052 cool-core cluster. The box at the lower left corner of each image shows the size of the $3''.7 \times 10''.0$ spectral extraction region at $10\mu\text{m}$.

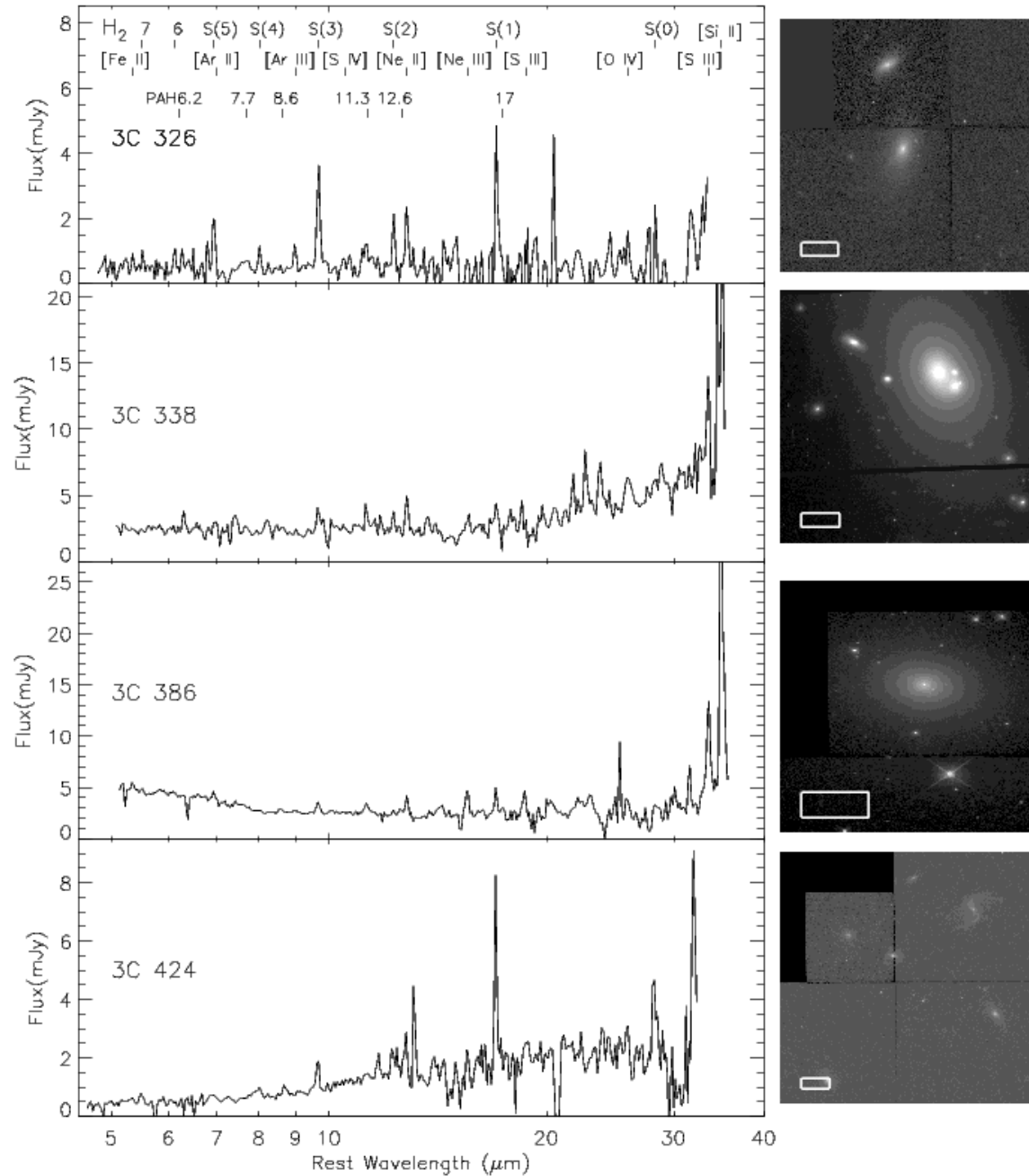


FIG. 3.— *Spitzer* IRS low-resolution spectra of 3C 326, 338, 386, and 424. These sources have weak PAH emission and no silicate absorption. HST WFPC2 and ACS images are to the right. The 3C 326 pair appears to be interacting (Ogle et al. 2007). Radio galaxy 3C 338 resides in the A 2199 cool core cluster, while 3C 386 is an isolated elliptical galaxy. The host of 3C 424 appears (centered on the smaller PC chip) in a rich group of galaxies. The box at the lower left corner of each image shows the size of the $3''.7 \times 10''.0$ spectral extraction region at $10 \mu\text{m}$.

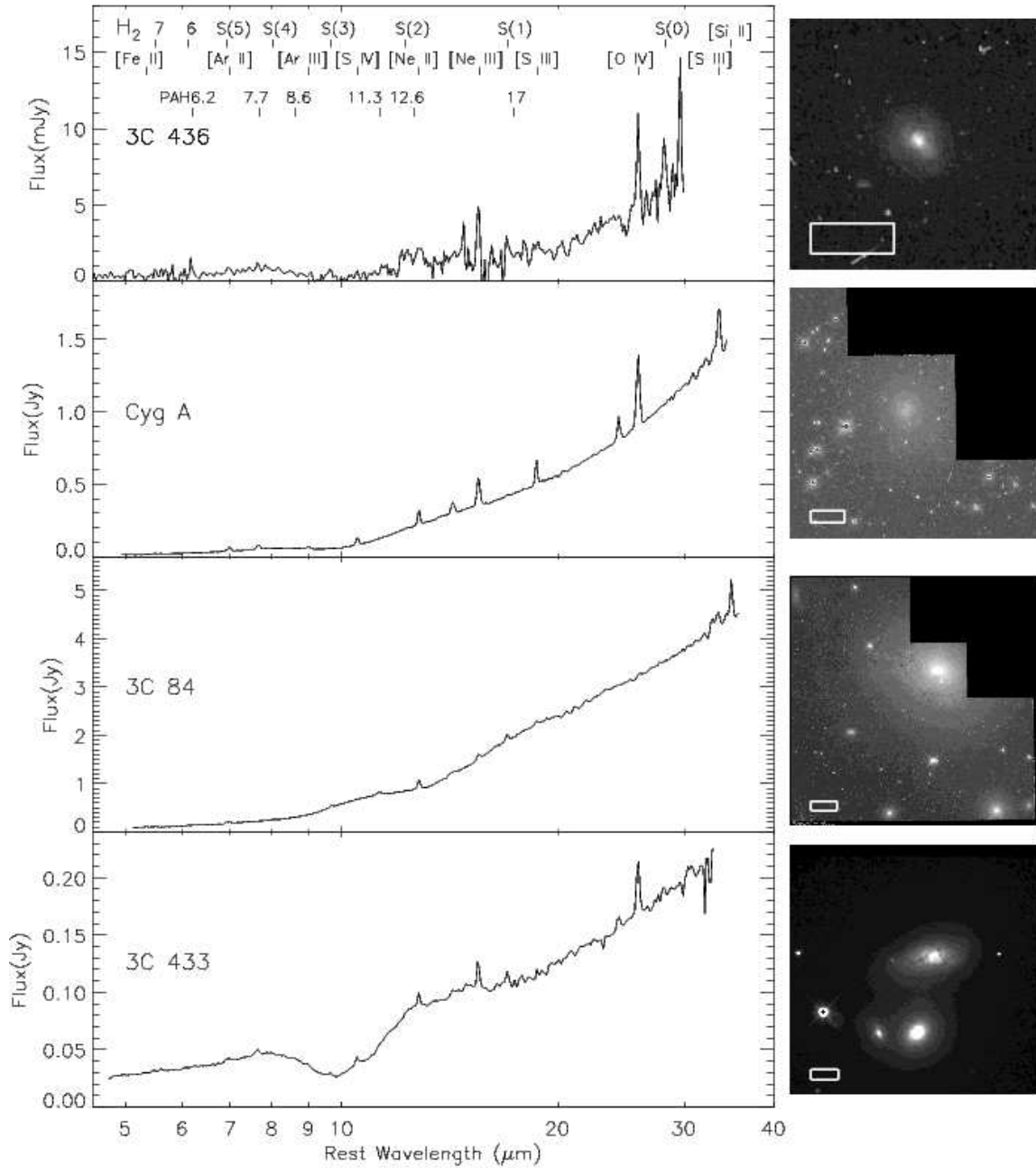


FIG. 4.— *Spitzer* IRS low-resolution spectra of 3C 436, Cyg A, 3C 84 (= Per A), and 3C 433. Silicate emission is seen at $10\ \mu\text{m}$ and $18\ \mu\text{m}$ in the Per A spectrum, and silicate absorption in 3C 436, 433, and Cyg A. HST WFPC2 images are at the right. Per A is interacting with an in-falling dusty companion seen in the foreground. The disk, dusty host of 3C 433 resides in an interacting group of 3 galaxies. The box at the lower left corner of each image shows the size of the $3''.7 \times 10''.0$ spectral extraction region at $10\ \mu\text{m}$. See Figs. 5 and 6 for spectral fits of 3C 84 and Cyg A.

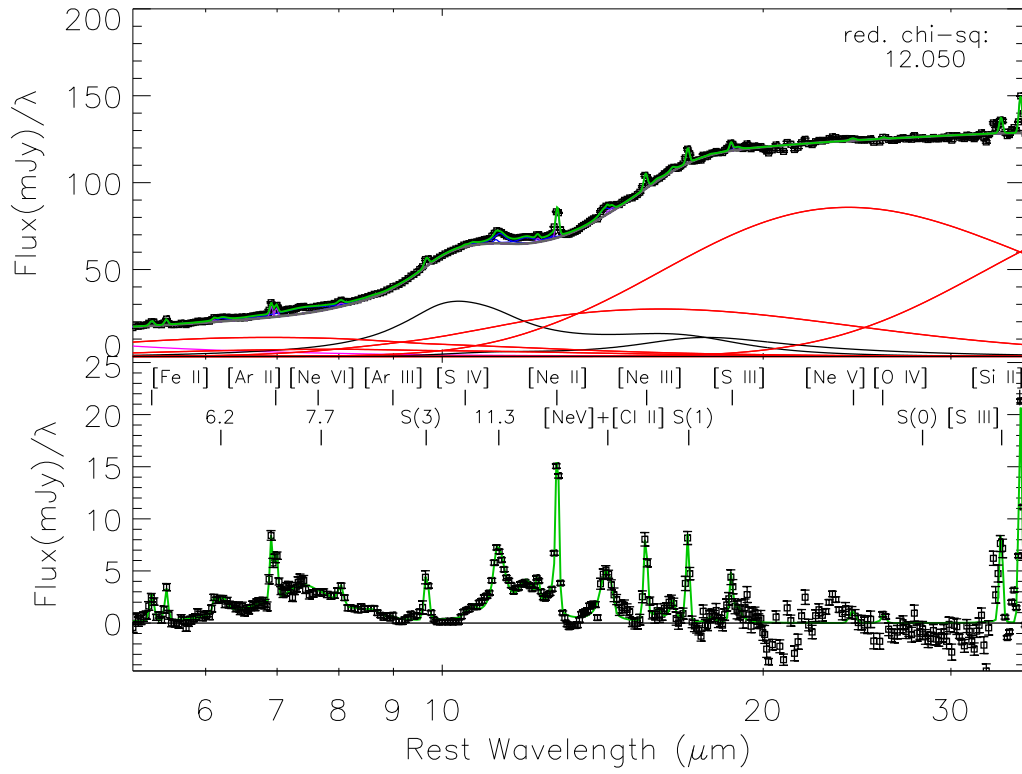


FIG. 5.— *Spitzer* IRS low-resolution spectrum of 3C 84 (= Per A), with best fit model and model components. Silicate emission at $10\ \mu\text{m}$ and $18\ \mu\text{m}$ is fit by a blackbody times an empirical AGN silicate dust emissivity curve. The bottom panel shows the continuum-subtracted PAH and emission line spectrum, including H_2 pure-rotational lines.

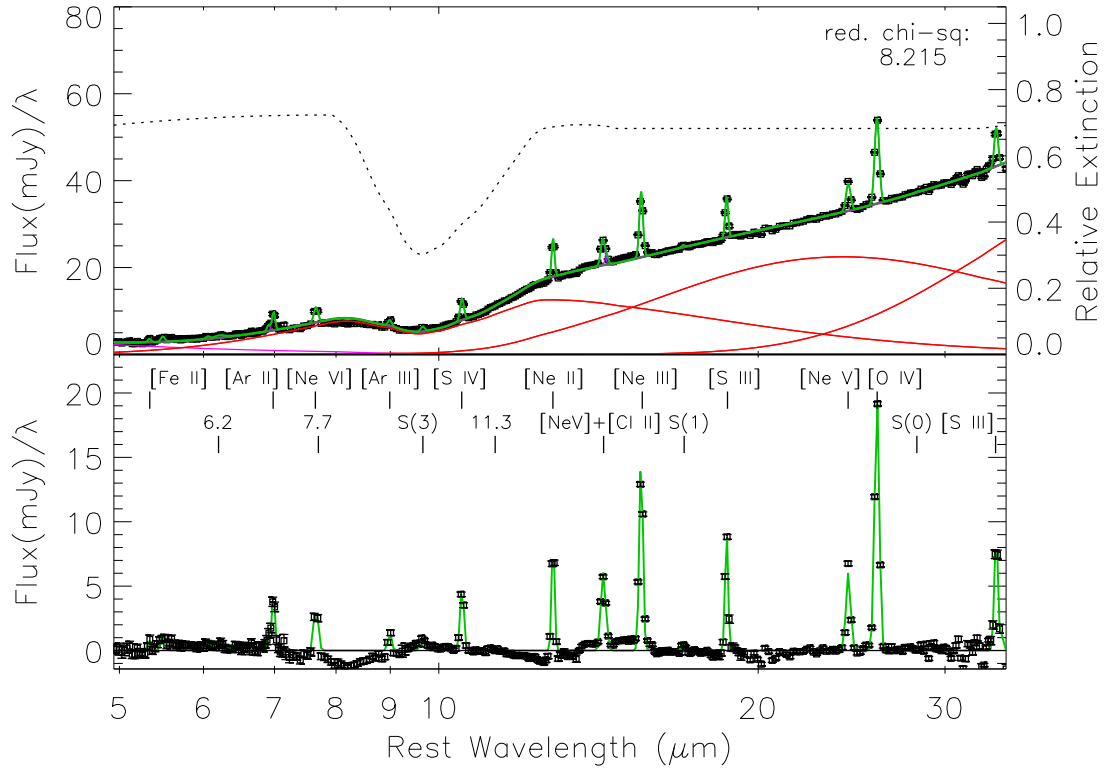


FIG. 6.— *Spitzer* IRS low-resolution spectrum of 3C 405 (= Cyg A), with best fit model and model components. A custom extinction curve (dotted line), lacking the $18\ \mu\text{m}$ silicate feature, was required to fit the continuum. The bottom panel shows the continuum-subtracted emission line spectrum, including H_2 pure-rotational lines.

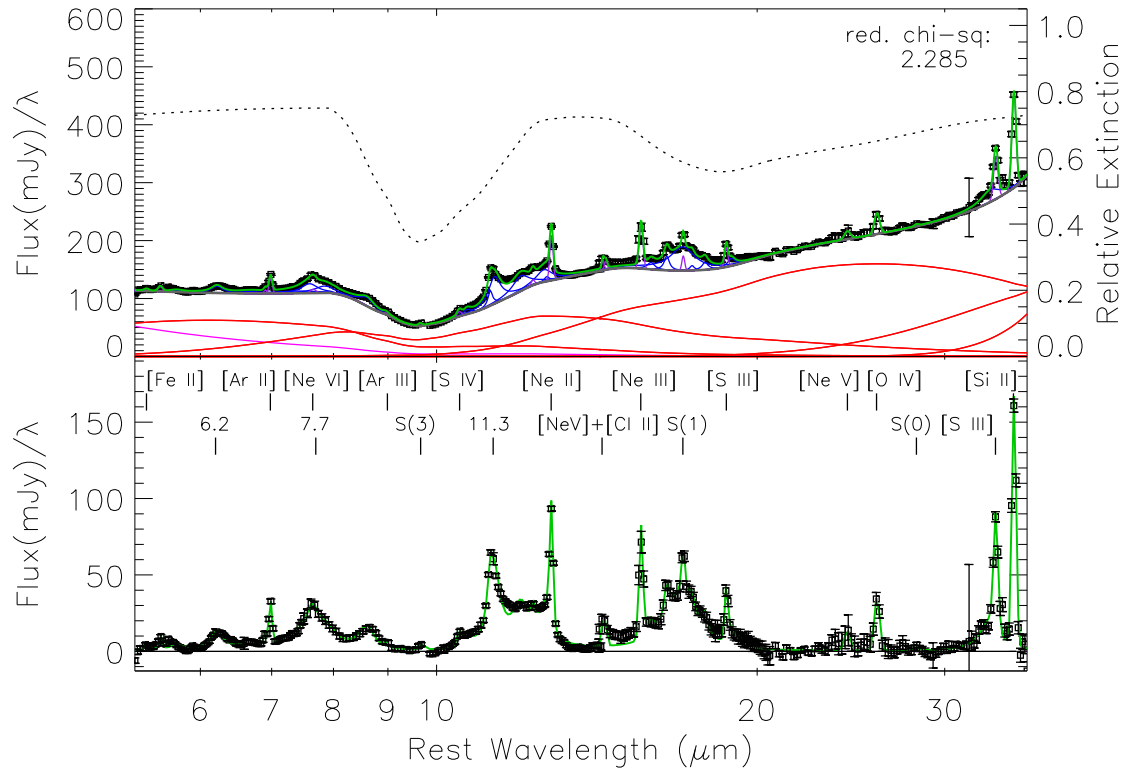


FIG. 7.— *Spitzer* IRS low-resolution spectrum of Cen A (= NGC 5128), with best fit model and model components. The bottom panel shows the continuum-subtracted PAH and emission line spectrum, including H_2 pure-rotational lines.

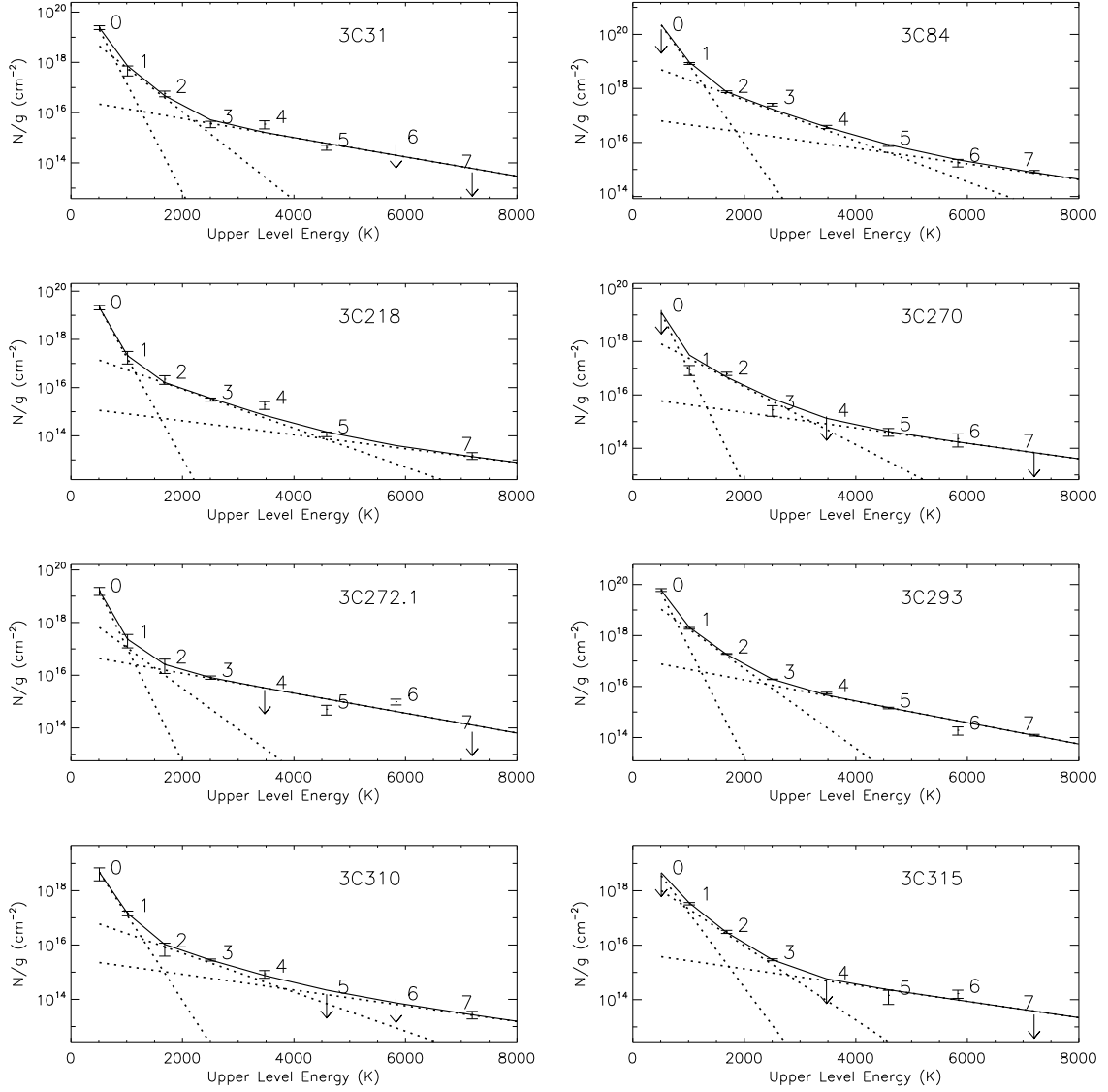


FIG. 8.— H_2 excitation diagrams. Upper level column density divided by statistical weight (for H_2 uniformly filling the SL slit width) or 2σ upper limit is plotted against upper level energy $E/k_b(K)$ for each H_2 0-0 S(J) pure-rotational emission line. Model H_2 temperature components (dotted lines) are listed in Table 11.

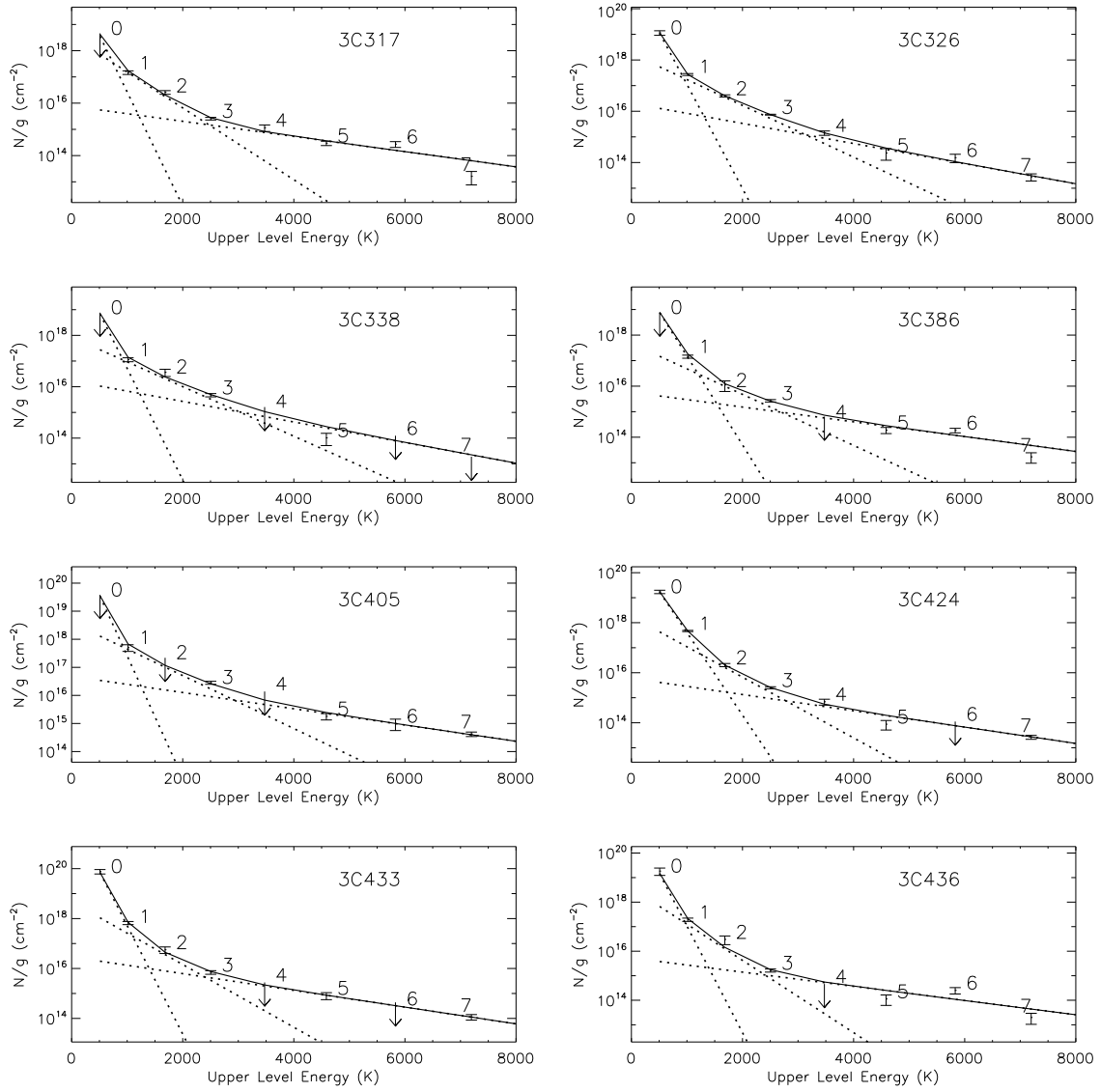


FIG. 9.— H_2 excitation diagrams. Upper level column density divided by statistical weight (for H_2 uniformly filling the SL slit width) or 2σ upper limit is plotted against upper level energy $E/k_b(\text{K})$ for each H_2 0-0 S(J) pure-rotational emission line. Model H_2 temperature components (dotted lines) are listed in Table 11.

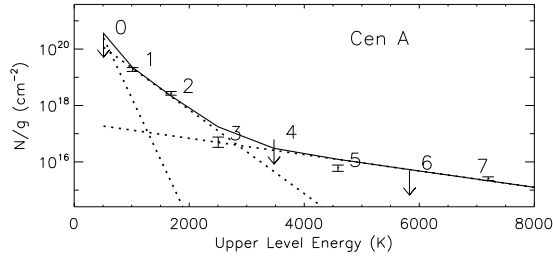


FIG. 10.— H₂ excitation diagram for Cen A. Upper level column density divided by statistical weight (for H₂ uniformly filling the SL slit width) or 2σ upper limit is plotted against upper level energy $E/k_b(K)$ for each H₂ 0-0 S(J) pure-rotational emission line. Model H₂ temperature components (dotted lines) are listed in Table 11.

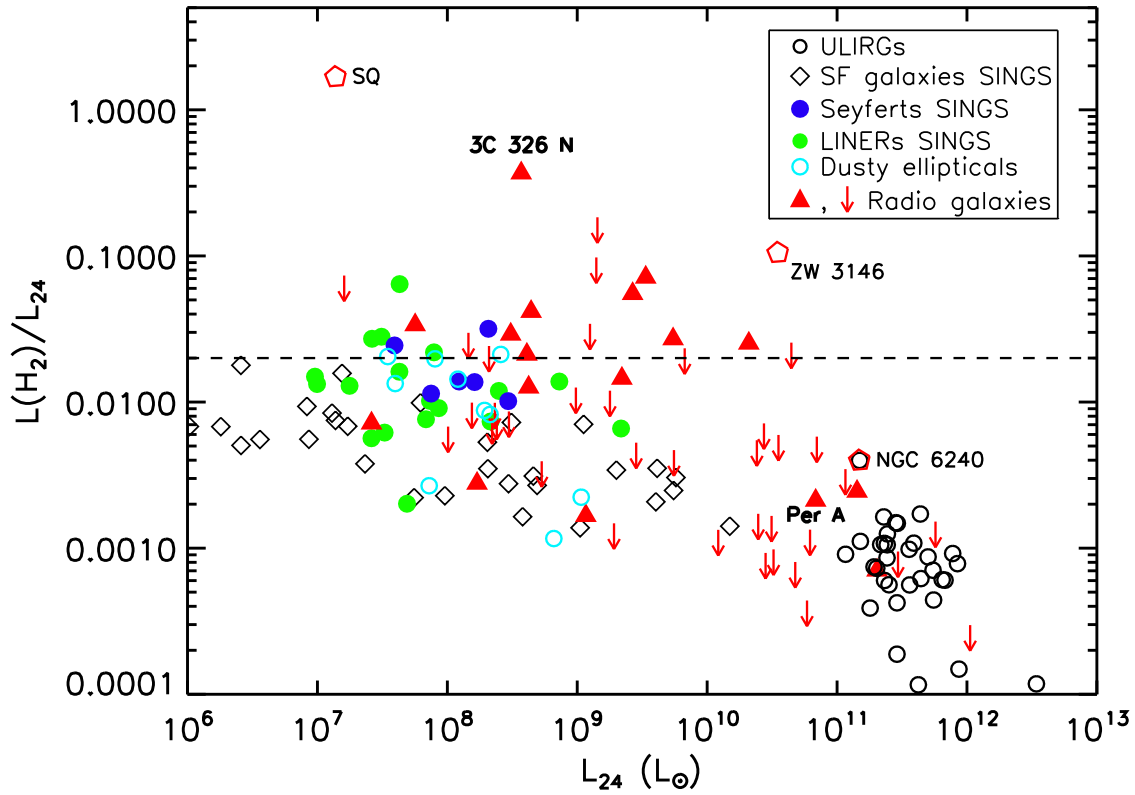


FIG. 11.— Ratio of H_2 luminosity summed over the 0-0 S(0)-S(3) pure rotational lines to $L_{24} = \nu L_\nu(24 \mu\text{m, rest})$ luminosity. Radio galaxies (this work) are compared to SINGS star-forming galaxies, Seyferts, and LINERs (Roussel et al. 2007), ULIRGs (Higdon et al. 2006), and the subset of Kaneda et al. (2008) dusty ellipticals that have $24 \mu\text{m}$ *Spitzer* MIPS fluxes (Temi et al. 2007). Radio galaxy H_2 upper limits (from Tables 2 and 6) are plotted as downward pointing arrows. The LIRG NGC 6240 (Armus et al. 2006), the Zw 3146 brightest cluster galaxy (Egami et al. 2006), and the Stephan's Quintet intergalactic shock (SQ shock sub-region, Cluver et al. 2010) are plotted for comparison. The large values of $L(H_2)/L_{24} > 0.02$ in many radio galaxies indicate the importance of non-radiative heating (e.g., shocks).

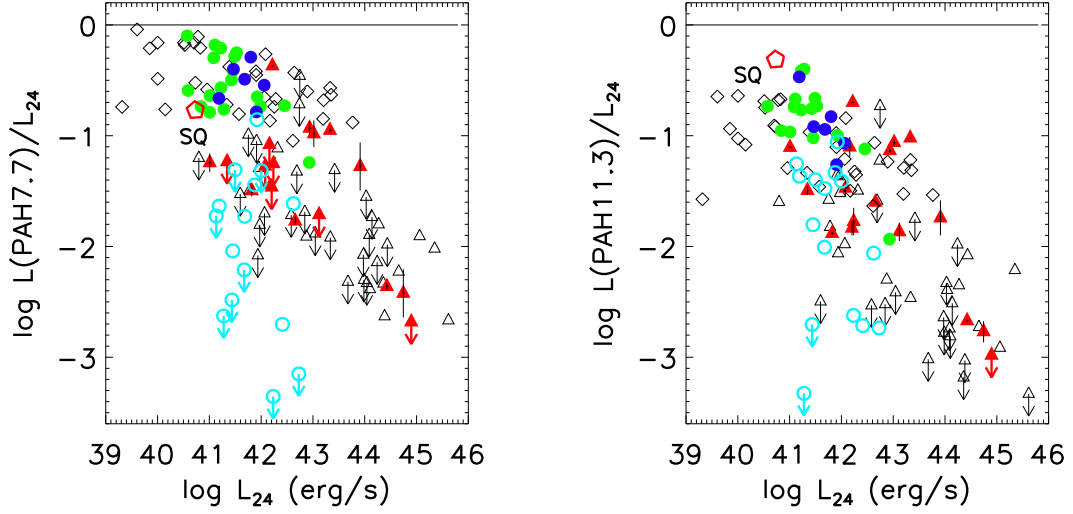


FIG. 12.— PAH to $\nu L_\nu(24 \mu\text{m}, \text{rest})$ luminosity ratio, for the 7.7 and 11.3 μm PAH features. (See Fig. 11 for symbol legend; H_2 nondetected radio galaxies are plotted as open triangles.) Solid line corresponds to 1:1 ratio. Radio galaxies (this work) are compared to SINGS star-forming galaxies, Seyferts, and LINERs (Roussel et al. 2007; Smith et al. 2007), the Kaneda et al. (2008) dusty ellipticals, and the Stephan's Quintet intergalactic shock (SQ shock sub-region, Cluver et al. 2010). Most radio galaxies have $L(\text{PAH}7.7)/L_{24} < 0.1$, indicating a very small star formation contribution and dominant AGN contribution to the mid-IR continuum.

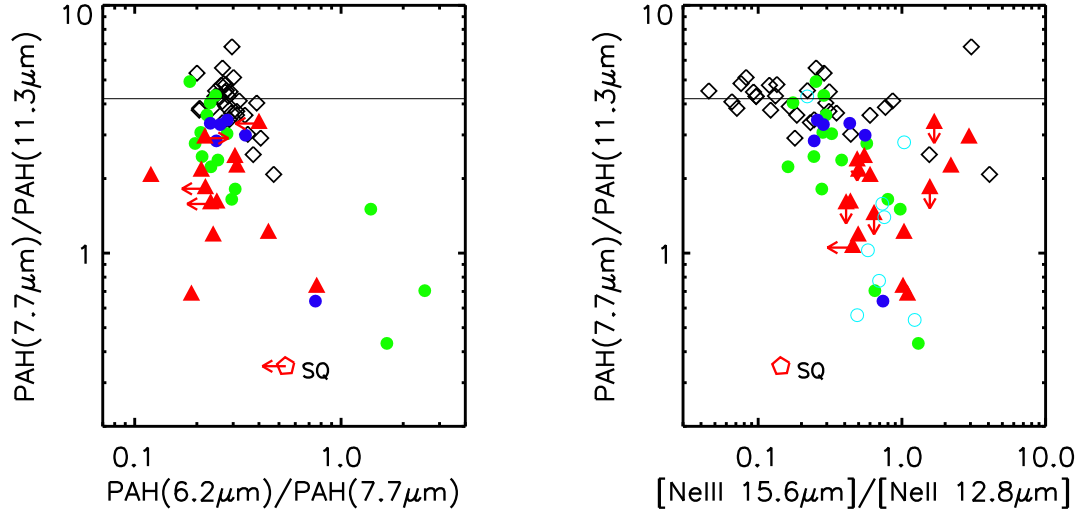


FIG. 13.— Left: PAH emission feature flux ratios (see Fig. 11 for symbol legend). H_2 -detected radio galaxies (triangles, this work) are compared to SINGS star-forming galaxies, Seyferts, and LINERs (Smith et al. 2007), the Kaneda et al. (2008) dusty ellipticals, and the Stephan's Quintet intergalactic shock (SQ shock sub-region, Cluver et al. 2010). Four radio galaxies with neither 6.2 μm nor 7.7 μm PAH detected are not plotted. The median $\text{PAH}(7.7 \mu\text{m})/\text{PAH}(11.3 \mu\text{m})$ ratio is lower in radio galaxies than in star-forming galaxies, while the median $\text{PAH}(6.2 \mu\text{m})/\text{PAH}(7.7 \mu\text{m})$ ratio is similar. This indicates lower PAH ionization caused by a weaker interstellar UV radiation field or increased gas-phase ionization by X-rays or cosmic rays. Right: $\text{PAH}(7.7 \mu\text{m})/\text{PAH}(11.3 \mu\text{m})$ vs. $[\text{Ne III}] 15.6 \mu\text{m}/[\text{Ne II}] 12.8 \mu\text{m}$ line flux ratio after Smith et al. (2007). One radio galaxy with no PAH features detected (3C 405) is not plotted. The large $[\text{Ne III}]/[\text{Ne II}]$ ratio relative to star-forming galaxies may be attributed to AGN activity.

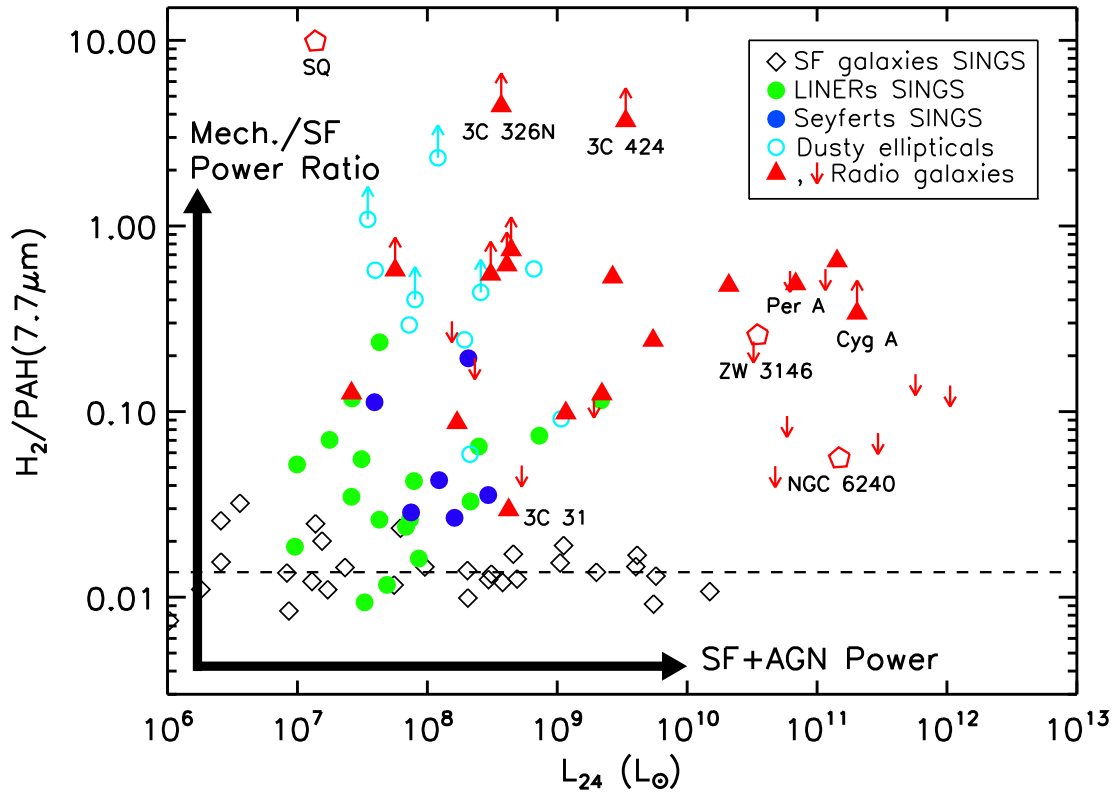


FIG. 14.— Ratio of H_2 luminosity summed over the 0-0 S(0)-S(3) lines to $7.7 \mu\text{m}$ PAH luminosity vs. $\nu L_\nu(24 \mu\text{m,rest})$ continuum luminosity. This ratio indicates the relative importance of mechanical heating and star formation power. All but one of the H_2 -detected radio galaxies from our sample stand out above normal star-forming galaxies from the SINGS survey (Roussel et al. 2007) and are MOHEGs, with $L(H_2)/L(\text{PAH}7.7) > 0.04$. Radio galaxy H_2 upper limits with detected $7.7 \mu\text{m}$ PAH emission (from Tables 2 and 6) are plotted as downward pointing arrows. Many of the LINERs and Seyferts from the SINGS sample (Roussel et al. 2007) and several of the Kaneda et al. (2008) dusty ellipticals are MOHEGs. Other MOHEGs from the literature, including NGC 6240 (Armus et al. 2006), Zw 3146 (Egami et al. 2006), and the Stephan’s Quintet intergalactic shock (SQ shock sub-region, Cluver et al. 2010), are plotted for comparison.

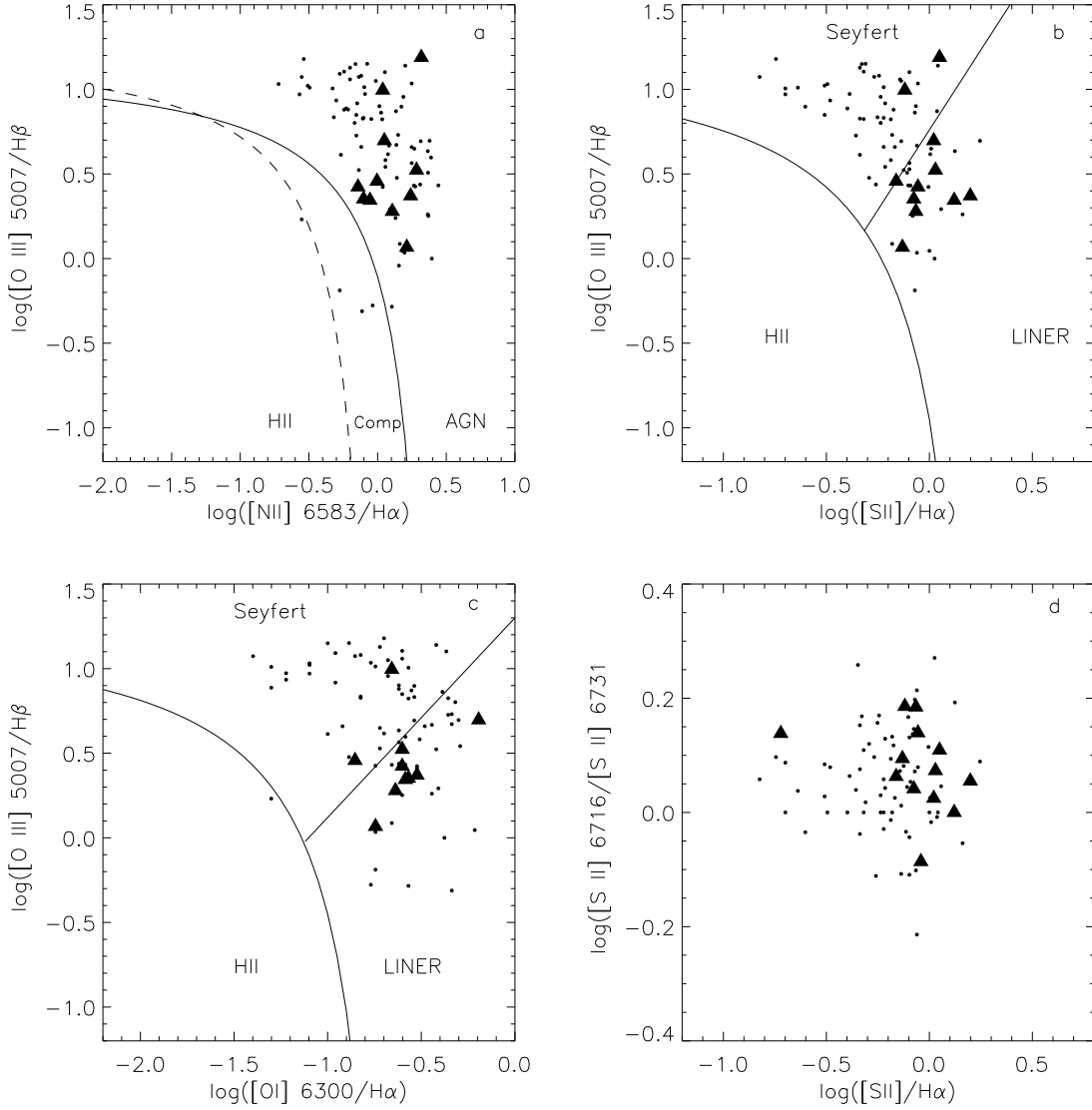


FIG. 15.— BPT (Baldwin et al. 1981) AGN diagnostic diagrams. a) The radio MOHEGs (filled triangles) have optical emission line ratios consistent with pure AGN, rather than star-forming (H II) or composite galaxies. Optical line fluxes for these galaxies and other $z < 0.3$ 3C radio galaxies (small dots) are from Buttiglione et al. (2009). b) and c) Nearly all radio MOHEGs on these plots (except 3C 433 and 436) are classified as LINERs according to the dividing lines of Kewley et al. (2006). d) The density-sensitive [S II] doublet ratio falls within the normal range for radio galaxies.

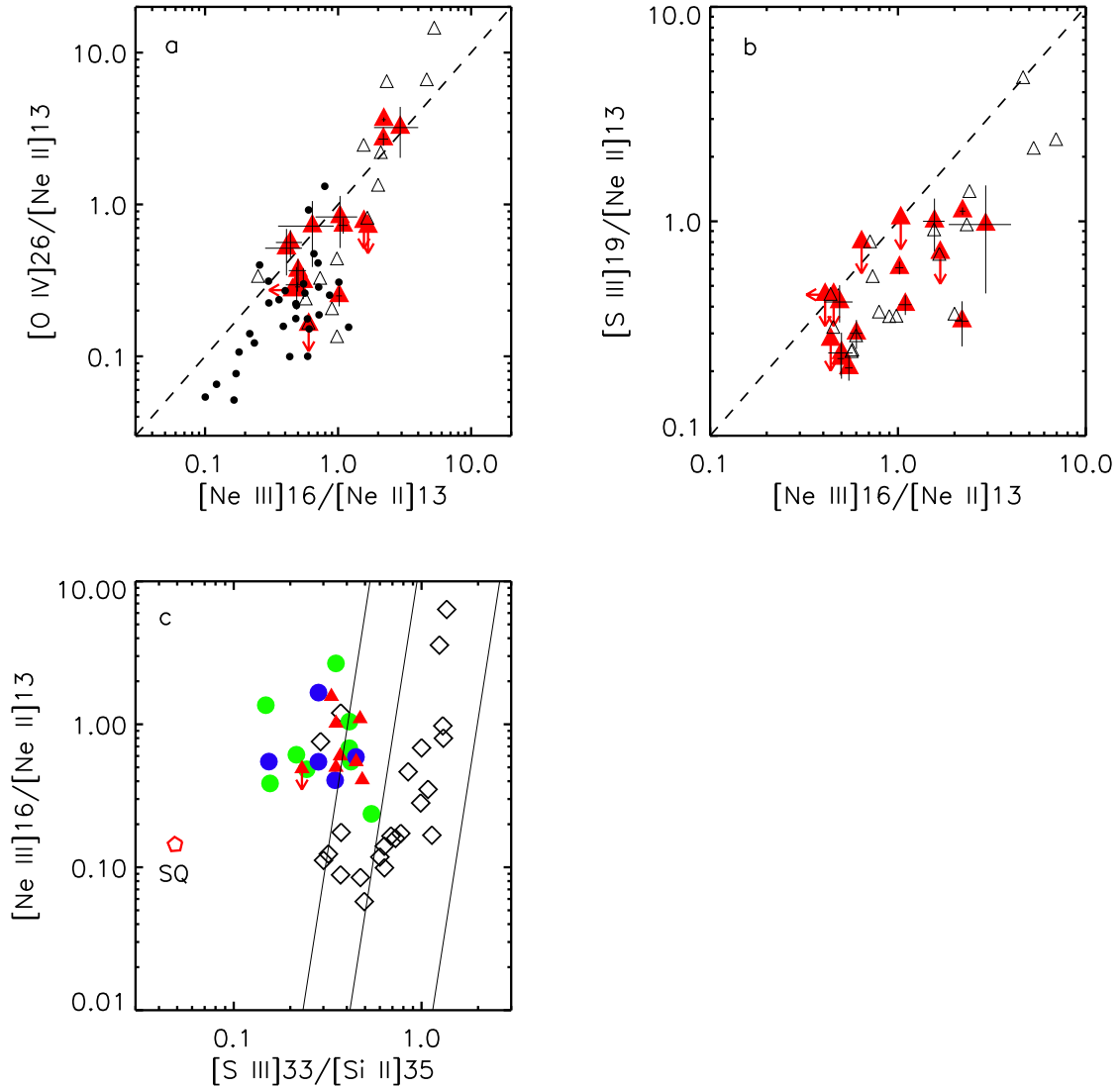


FIG. 16.— a,b) The mid-IR forbidden line ratios of radio MOHEGs (filled triangles) and H₂ undetected radio galaxies (open triangles). The dashed lines correspond to a 1:1 ratio of ratios. Other LINERs measured by *Spitzer* (Dudik et al. 2009, small dots) are shown for comparison in the first panel. c) Dale et al. (2006) MIR forbidden line diagnostic diagram (see Fig. 14 for symbol legend). The line ratios of radio MOHEGs with [Si II] measured are consistent with LINERs and Seyferts, but segregate from star-forming galaxies in the SINGS survey (Smith et al. 2007). The Stephan’s Quintet intergalactic shock (red pentagon, SQ shock sub-region, Cluver et al. 2010) has lower ionization than radio MOHEGs.

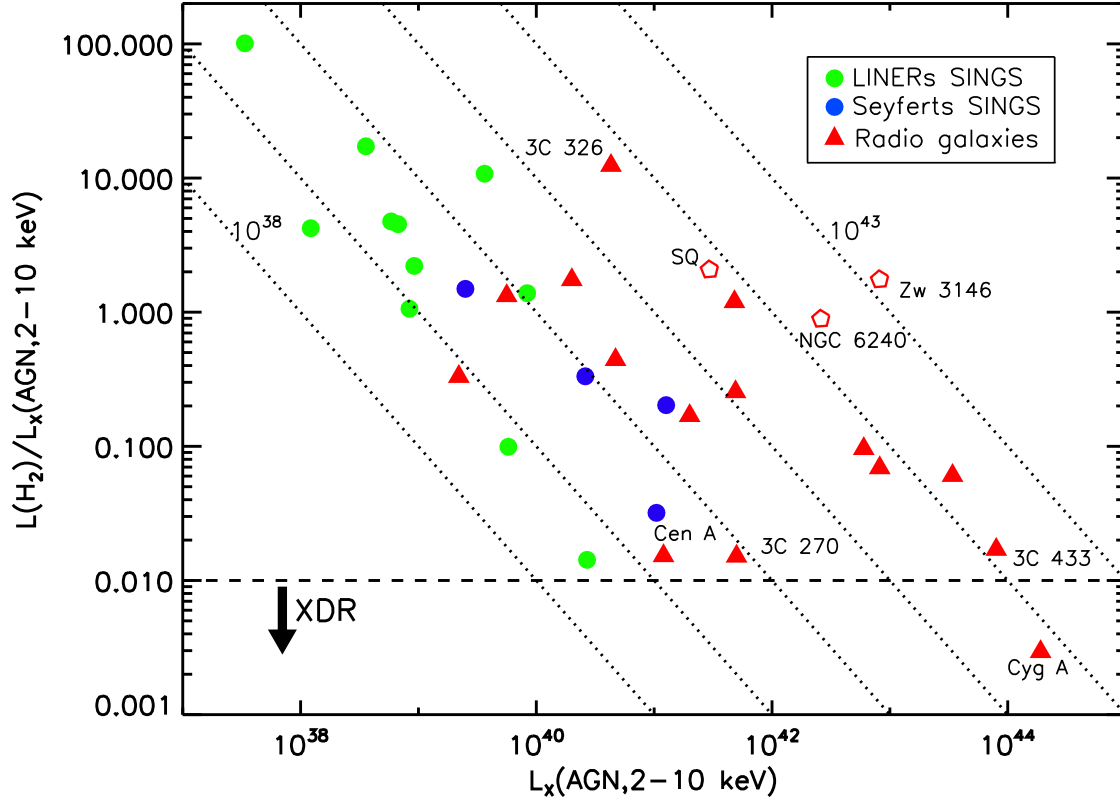


FIG. 17.— Ratio of H_2 luminosity (summed over 0-0 S(0)-S(3)) to unabsorbed AGN X-ray (2-10 keV) luminosity. For Stephan's Quintet (SQ main shock, Cluver et al. 2010), the H_2 and X-ray luminosities (0.001-10 keV) are integrated over the entire main shock region. For NGC 6240, the X-ray luminosity (0.1-10 keV) is the total for the binary AGN (Komossa et al. 2003). There is likely significant contamination to the X-ray luminosity of Zw 3146 from the surrounding galaxy cluster. Two radio galaxies (3C 310 and 424) that have not been observed by *Chandra* are not plotted. Diagonal dotted lines indicate constant $L(H_2)$. The horizontal dashed line indicates the 1% maximum H_2 to X-ray luminosity ratio for an X-ray dissociation region (XDR) at the characteristic observed H_2 temperature of 200 K. The H_2 emission from all radio MOHEGs (except Cyg A) and SINGS AGNs is too luminous to be powered by X-rays from the active nuclei.

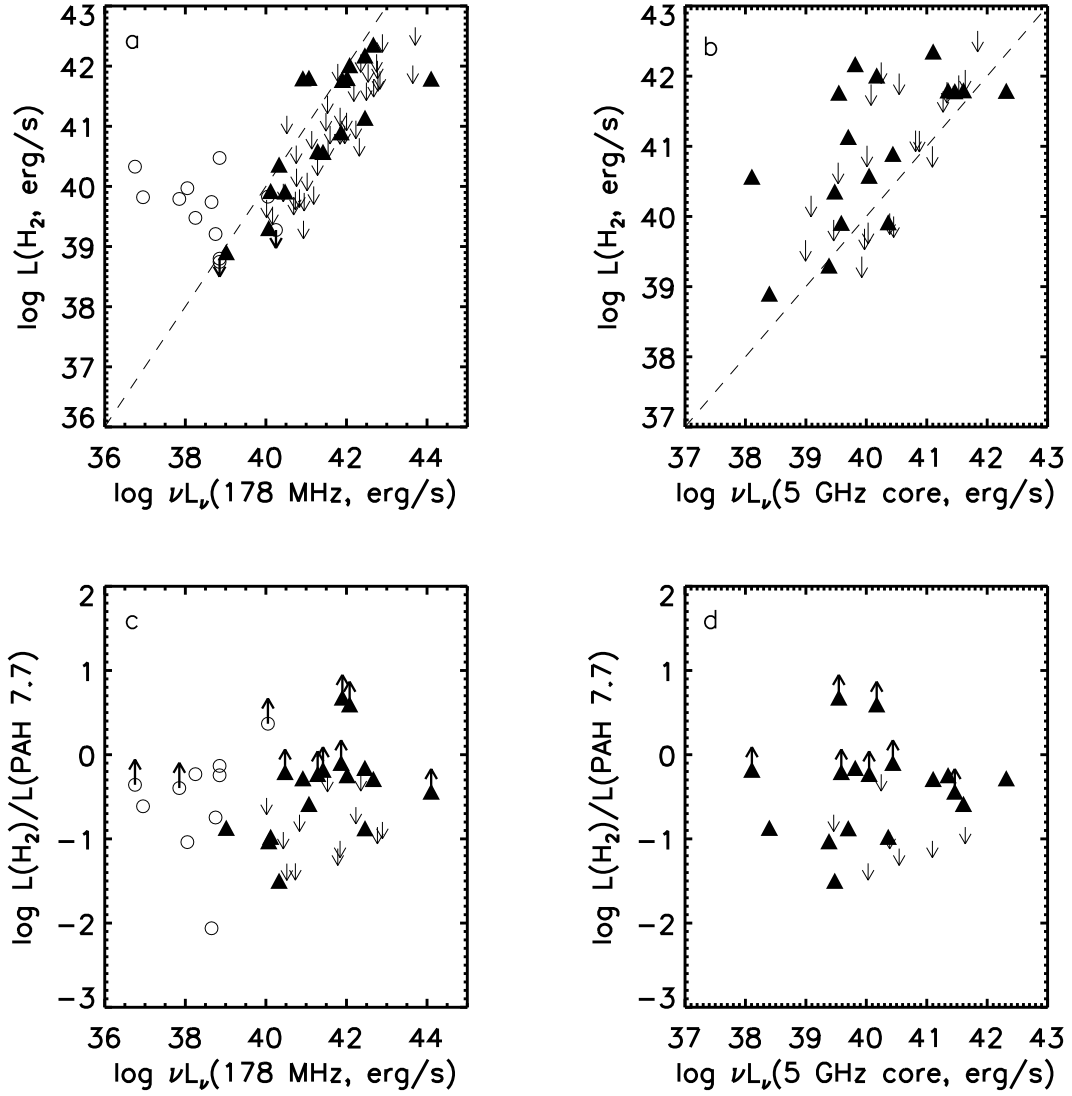


FIG. 18.— a,b) H₂ luminosity (summed over 0-0 S(0)-S(3)) vs. radio luminosity at 178 MHz and arcsecond-scale radio core luminosity at 5 GHz (<http://3crr.extragalactic.info/cgi/database>). Radio MOHEGs (filled triangles), H₂ nondetected radio galaxies (downward arrows), and Kaneda et al. (2008) dusty ellipticals (open circles) are shown. Dashed lines correspond to 1:1 ratio. c,d) H₂ over 7.7 μm PAH luminosity ratio vs. radio luminosity at 178 MHz and arcsecond-scale radio core luminosity at 5 GHz.

TABLE 1
H₂ DETECTED RADIO GALAXIES (RADIO MOHEGS)

Source	Morph. ^a	Sp.T. ^b	<i>z</i>	<i>F</i> ₂₄ ^c	S178 ^d	Ref. ^e
3C 31	I,TJ	LIG	0.01701	19.9±0.3	18.3	1
3C 84	I,FD	LIG	0.01756	3020.±30.	66.8	1
3C 218	I,TJ	LIG	0.05488	9.1±0.2	225.7	4
3C 270	I,TJ	LIG	0.007465	42.4±0.4	53.4	2
3C 272.1	I,TJ	LIG	0.003536	29.4±0.2	21.1	1
3C 293	I,CSC	LIG	0.04503	34.3±1.0	13.8	1
3C 317	I,FD	LIG	0.03446	4.5±0.1	53.4	3
3C 338	I _p ,FD	LIG	0.03035	4.4±0.3	51.1	3
3C 386	I,FD	LIG	0.01689	2.7±0.4	26.1	1
3C 424	I,DD	LIG	0.1270	2.2±0.1	15.9	3
Cen A	I,TJ	LIG	0.001825	4950.±110.	1005.	4
3C 310	II,FD	LIG	0.0538	1.9±0.2	60.1	1
3C 315	II,X,CSC	HIG	0.1083	2.5±0.1	19.4	1
3C 326 N	II	LIG	0.0895	0.53±0.12	22.2	1
3C 405	II	HIG	0.05608	800.±20.	9483.	3
3C 433	II,X	HIG	0.1016	154.± 3.	61.3	1
3C 436	II	HIG	0.2145	4.0±0.1	19.4	1

^a Radio morphologies: I or II = Fanaroff & Riley (1974) type (p = peculiar), TJ = twin jet, FD = fat double, CSC = compact symmetric core, DD = double-double, X = 'X'-shaped, SJ = single (one-sided) jet.

^b Optical spectral type: LIG = low ionization narrow line galaxy, HIG = high ionization narrow line galaxy, BLRG = broad line radio galaxy.

^c Rest 24 μm flux (mJy) measured with *Spitzer* IRS. A 3.7σ-clipped average over 22.5-25.5 μm was used, removing any large noise spikes or contributions from the [Ne v] 24.31 μm line.

^d The 178 MHz flux density (Jy) on Baars et al. (1977) scale.

^e References for 178 MHz flux density. (1) Laing et al. (1983) (2) Kuhr et al. (1981) (3) Kellermann et al. (1969) (4) Estimated from Kuhr et al. (1981) 160 MHz flux density.

TABLE 2
H₂ NONDETECTED RADIO GALAXIES

Source	Morph. ^a	Sp.T. ^b	<i>z</i>	<i>F</i> ₂₄ ^c	S178 ^d	Ref. ^e
3C 15	I	LIG	0.0730	12.4±0.3	16.9	2
3C 29	I,TJ	LIG	0.045031	11.2±0.3	16.2	2
3C 66B	I,TJ	LIG	0.02126	6.6±0.1	26.8	1
3C 76.1	I,FD	LIG	0.03249	2.6±0.2	13.3	1
3C 83.1	I	LIG	0.02514	4.9±0.1	26.6	1
3C 120	I,SJ	BLRG	0.03301	573.±5.	7.4	2
3C 129	I,TJ	LIG	0.0208	7.5±0.2	51.1	3
3C 189	I,TJ	LIG	0.04284	6.8±0.1	7.4	2
3C 264	I,TJ	LIG	0.02172	15.2±0.3	28.3	1
3C 274	I,TJ	LIG	0.004360	75.±1.	1145.	1
3C 318.1	I	LIG	0.04531	0.9±0.2	12.3	3
3C 348	I,TJ	LIG	0.1540	0.6±0.2	387.	2
3C 403.1	I	LIG	0.0554	< 0.2	14.7	3
3C 449	I,TJ	LIG	0.017085	0.75±0.11	12.5	1
3C 465	I,TJ	LIG	0.03022	4.3±0.2	41.2	1
NGC 6251	Ip	LIG	0.02471	42.±2.	10.9	1
IC 4296	Ip,DD	LIG	0.01247	13.7±0.2	16.8	2
3C 17	IIp	BLRG	0.219685	12.6±0.4	22.2	2
3C 28	II	LIG	0.1953	< 0.3	17.8	1
3C 33	II	HIG	0.0597	97.1±0.8	59.3	1
3C 61.1	II	HIG	0.1878	7.2±0.3	34.0	1
3C 111	II	BLRG	0.0485	168.±1.	70.4	3
3C 123	IIp	LIG	0.2177	8.2±0.2	206.0	1
3C 192	II	HIG	0.0597	9.8±0.4	23.0	1
3C 219	II	BLRG	0.1744	11.1±0.1	44.9	1
3C 234	II	HIG	0.1848	289.±1.	34.2	1
3C 319	II	LIG	0.1920	0.35±0.10	16.7	1
3C 321	II	HIG	0.0961	360.±10.	14.7	1
3C 346	II,FD	HIG	0.1620	9.0±0.1	11.9	1
3C 381	II	HIG	0.1605	44.2±0.5	18.1	1
3C 382	II	BLRG	0.0579	91.±2.	21.7	1
3C 388	II	LIG	0.0917	1.7±0.1	26.8	1
3C 390.3	II	BLRG	0.0561	231.±1.	51.8	1
3C 401	II	LIG	0.2011	1.5±0.1	22.8	1
3C 445	II	BLRG	0.0562	243.±2.	25.2	2
3C 452	II	HIG	0.0811	57.6±0.3	59.3	1
3C 459	II	HIG	0.2199	103.±3.	30.8	2
Pic A	II	BLRG	0.03506	129.±2.	411.	4

^a Radio morphology (see Table 1 for key).

^b Optical spectral type (see Table 1 for key).

^c Rest 24 μ m flux (mJy) or 2σ upper limit measured with *Spitzer* IRS. A 3.7σ -clipped average over 22.5-25.5 μ m was used, removing any large noise spikes or contributions from the [Ne v] 24.31 μ m line.

^d The 178 MHz flux density (Jy) on Baars et al. (1977) scale.

^e References for 178 MHz flux density. (1) Laing et al. (1983). (2) Kuhr et al. (1981) (3) Kellermann et al. (1969) (4) Estimated from Kuhr et al. (1981) 160 MHz flux density.

TABLE 3
 RADIO MOHEG HOST, ENVIRONMENT, AND INTERACTIONS

Source	Name	NGC	Host ^a	Dust Morph. ^b	Environment ^c	Interaction ^d
3C 31		383	Ep	disk	Arp 331 group	close companion
3C 84	Per A	1275	cD+D	complex	Perseus CC cluster	infalling spiral
3C 218	Hyd A		cD		A 780 CC cluster	close companion
3C 270		4261	Ep	disk	Virgo cluster	tail
3C 272.1	M 84	4374	Ep	lanes	Virgo cluster	
3C 293			S0	lanes	pair	bridge,tail
3C 310			Ep+D		poor cluster	bridge
3C 315			S0	lane	pair	close companion
3C 317			cD+D	filaments	A2052 CC cluster	close companion
3C 326 N			Ep+D		pair	bridge,tail
3C 338		6166	cD	filaments	A2199 CC cluster	nest
3C 386			E		single	
3C 405	Cyg A		Ep	complex	Cyg A cluster	merger
3C 424			Ep		group	
3C 433			S0	complex	group	bridge, nest
3C 436			Ep	lane	single	merger
Cen A		5128	Ep	lanes	single	merger

^a Host morphology. E= elliptical, Ep= peculiar elliptical, cD = cluster dominant, S0 = lenticular. The tag '+D' indicates a significant exponential disk component in the near-IR radial light profile (Donzelli et al. 2007).

^b Dust morphology, after (De Koff et al. 2000).

^c Cluster, group, or pair membership. CC cluster = cool X-ray core cluster.

^d Qualitative assessment of tidal interactions including close companion, tail, bridge, or merger. 'Nest' indicates multiple galaxies surrounded by a common envelope.

TABLE 4
RADIO MOHEG H₂ 0-0 S(J) EMISSION LINES

Source	H ₂ S(0) 28.22 μm	H ₂ S(1) 17.03 μm	H ₂ S(2) 12.28 μm	H ₂ S(3) 9.66 μm	H ₂ S(4) 8.03 μm	H ₂ S(5) 6.91 μm	H ₂ S(6) 6.11 μm	H ₂ S(7) 5.55 μm
3C 31	0.64(0.11)	1.36(0.58)	0.59(0.15)	0.60(0.17)	0.76(0.27)	0.80(0.18)	< 0.9	< 0.4
3C 84	< 4.	25. (2.)	6.7 (0.5)	43. (5.)	8.2 (1.1)	15. (1.)	2.9 (0.9)	8.8 (0.9)
3C 218	0.55(0.11)	0.41(0.22)	0.23(0.09)	0.55(0.08)	0.42(0.15)	0.23(0.05)	...	0.16(0.05)
3C 270	< 0.4	0.27(0.11)	0.57(0.08)	0.47(0.20)	< 0.3	0.81(0.26)	0.37(0.19)	< 0.7
3C 272.1	0.42(0.14)	0.55(0.29)	0.27(0.15)	1.4 (0.2)	< 0.6	1.0 (0.4)	1.6 (0.4)	< 0.6
3C 293	1.6 (0.2)	5.3 (0.4)	1.94(0.07)	3.25(0.07)	1.2 (0.1)	2.8 (0.2)	0.31(0.11)	1.3 (0.1)
3C 310	0.12(0.06)	0.36(0.07)	0.08(0.04)	0.48(0.04)	0.19(0.06)	< 0.3	< 0.14	0.29(0.09)
3C 315	< 0.12	1.0 (0.1)	0.30(0.04)	0.50(0.04)	< 0.11	0.28(0.15)	0.27(0.09)	< 0.3
3C 317	< 0.12	0.44(0.07)	0.25(0.04)	0.44(0.05)	0.25(0.07)	0.58(0.11)	0.44(0.11)	0.17(0.09)
3C 326 N	0.30(0.06)	0.69(0.06)	0.41(0.04)	1.26(0.05)	0.31(0.06)	0.46(0.22)	0.25(0.09)	0.29(0.09)
3C 338	< 0.2	0.34(0.06)	0.32(0.10)	0.81(0.12)	< 0.3	0.20(0.10)	< 0.2	< 0.2
3C 386	< 0.2	0.43(0.06)	0.09(0.04)	0.46(0.05)	< 0.11	0.37(0.10)	0.30(0.06)	0.18(0.07)
3C 405	< 1.0	1.5(0.4)	< 1.9	4.1 (0.5)	< 3.	3.5 (0.9)	1.6 (0.7)	4.4 (0.8)
3C 424	0.45(0.07)	1.12(0.06)	0.21(0.03)	0.43(0.04)	0.15(0.04)	0.17(0.07)	< 0.18	0.28(0.05)
3C 433	2.0 (0.4)	1.4 (0.2)	0.58(0.17)	1.2 (0.2)	< 0.6	1.6 (0.5)	< 0.5	1.2 (0.3)
3C 436	0.48(0.16)	0.46(0.07)	0.31(0.12)	0.28(0.04)	< 0.10	0.22(0.10)	0.41(0.12)	0.21(0.10)
Cen A	10. (6.)	57. (9.)	27. (4.)	9.3(3.7)	< 13.	12. (3.)	< 8.	27. (4.)

NOTE. — H₂ pure rotational line fluxes (10^{-14} erg s⁻¹ cm⁻²) or 2σ upper limits measured with *Spitzer* IRS, with 1σ uncertainties in parentheses. The 3C 218 H₂ S(6) line was unmeasurable owing to a large instrumental noise spike.

TABLE 5
RADIO MOHEG PAH FEATURES

Source	6.2 μm	7.7 μm	8.6 μm	11.3 μm	12.0 μm	12.6 μm	17 μm
3C 31	22.7(0.5)	108.(2.)	20.0(0.8)	50.5(0.5)	16.4(0.7)	27.3(0.7)	28.4(1.0)
3C 84	20. (3.)	167.(12.)	19. (3.)	82. (2.)	61. (2.)	34. (3.)	38. (10.)
3C 218	3.5(0.2)	14.(2.)	4.0(0.5)	8.8(0.4)	< 0.8	3.9(0.5)	2.8(1.3)
3C 270	5.2(0.6)	17.(2.)	< 0.9	7.0(0.2)	5.7(0.4)	4.1(0.4)	< 0.5
3C 272.1	16. (1.)	21.(4.)	< 6.	28.9(0.5)	5.2(0.6)	11.4(0.7)	22.1(1.4)
3C 293	12.0(0.6)	50.(2.)	21.9(0.6)	42.7(0.5)	14.4(0.5)	23.6(0.6)	26.2(1.5)
3C 310	0.56(0.28)	< 1.4	< 0.3	0.42(0.12)	0.29(0.13)	0.15(0.06)	< 0.3
3C 315	1.6(0.4)	3.6(1.0)	0.52(0.23)	3.0(0.2)	0.87(0.22)	1.9(0.3)	4.8(0.6)
3C 317	< 1.3	< 2.	< 0.8	0.85(0.13)	0.92(0.20)	1.3(0.2)	1.5(0.4)
3C 326 N	< 0.5	< 0.6	< 0.4	0.57(0.12)	< 0.3	< 0.2	< 0.7
3C 338	0.70(0.32)	< 3.	< 1.0	1.9(0.3)	1.0(0.4)	< 0.8	< 0.8
3C 386	0.44(0.21)	< 2.	< 0.6	1.1(0.1)	< 0.4	0.72(0.18)	< 0.7
3C 405	< 6.	< 22.	< 6.	< 11.	< 14.	< 12.	< 14.
3C 424	< 0.3	< 0.6	< 0.2	0.42(0.08)	0.57(0.11)	0.87(0.15)	< 0.6
3C 433	2.5(1.1)	8. (4.)	9. (1.)	3.6(0.8)	9.5(1.0)	13. (1.)	32. (2.)
3C 436	< 0.7	3.2(1.6)	< 0.8	1.1(0.4)	< 1.4	2.1(0.7)	< 1.6
Cen A	198.(17.)	1052.(92.)	459.(32.)	1557.(26.)	848.(24.)	655.(27.)	2668.(73.)

NOTE. — Flux (10^{-14} erg s⁻¹ cm⁻²) or 2σ upper limit measured with *Spitzer* IRS and PAHFIT, with 1σ uncertainties in parentheses.

TABLE 6
H₂ UPPER LIMITS OR SINGLE-LINE DETECTIONS AND PAH FEATURES

Source	H ₂ S(0)	H ₂ S(1)	H ₂ S(2)	H ₂ S(3)	PAH 6.2 μm	PAH 7.7 μm	PAH 11.3 μm
3C 15	< 0.4	< 0.4	< 0.10	< 0.09	< 0.9	< 2.	0.57 (0.13)
3C 29	0.55(0.15)	< 0.7	< 0.2	< 0.4	< 0.9	< 3.	< 0.44
3C 66B	< 0.12	0.30(0.07)	< 0.10	< 0.11	< 0.5	< 0.7	0.73 (0.10)
3C 76.1	< 0.2	0.45(0.09)	< 0.12	< 0.06	< 1.3	< 3.	1.48 (0.11)
3C 83.1	< 0.14	< 0.14	< 0.11	0.25(0.06)	1.5 (0.5)	3.2 (1.6)	2.7 (0.2)
3C 120	< 2.2	2.74(0.75)	< 1.5	< 1.0	7.9 (2.0)	117. (14.)	33. (2.)
3C 129	< 0.3	< 0.19	< 0.16	0.31(0.08)	< 0.9	< 1.5	2.9 (0.2)
3C 189	0.23(0.08)	< 0.4	< 0.11	< 0.3	< 1.3	< 1.7	< 0.26
3C 264	< 0.3	0.28(0.12) ^a	< 0.11	0.20(0.05)	7.6 (0.5)	14.9 (1.7)	6.2 (0.2)
3C 274	< 0.7	< 1.1	< 1.6	2.92(0.62)	< 7.	< 28.	< 3.
3C 318.1	< 0.14	< 0.16	< 0.06	< 0.06	< 0.7	< 1.2	0.31 (0.07)
3C 348	< 0.4	< 0.5	< 0.4	< 0.5	< 2.	< 3.	< 1.6
3C 403.1	< 0.2	< 0.16	< 0.08	0.10(0.03)	< 0.4	< 1.1	0.65 (0.10)
3C 449	< 0.09	< 0.4	< 0.08	< 0.04	< 0.2	< 0.6	0.24 (0.07)
3C 465	< 0.18	< 0.2	< 0.07	< 0.10	< 0.4	< 1.1	0.58 (0.10)
NGC 6251	< 0.3	< 0.3	< 0.18	< 0.2	1.6 (0.2)	6.6 (1.0)	2.7 (0.2)
IC 4296	< 0.3	< 0.3	< 0.2	0.78(0.15)	< 3.	5.6 (1.0)	2.6 (0.3)
3C 17	< 0.4	< 0.5	< 0.5	< 0.2	< 1.2	< 2.	1.6 (0.3)
3C 28	< 0.3	< 0.4	< 0.4	0.22(0.04)	< 1.8	< 1.2	5.8 (0.6)
3C 33	< 0.7	< 0.5	< 0.19	0.25(0.09)	< 2.	< 6.	5.2 (0.4)
3C 61.1	< 0.3	0.37(0.10)	< 0.12	< 0.11	< 1.4	< 3.	< 0.5
3C 111	< 1.2	< 1.4	< 1.4	< 0.9	< 6.	< 28.	< 4.
3C 123	< 0.4	< 1.7	< 0.7	< 0.3	< 1.7	< 0.9	< 1.3
3C 192	< 0.2	< 0.3	< 0.16	< 0.13	< 1.1	< 1.7	< 0.5
3C 219	< 0.3	0.45(0.09)	< 0.3	< 0.16	1.9 (0.6)	< 3.	< 0.5
3C 234	< 1.9	... ^b	< 0.9	< 0.4	4.6 (1.6)	9.2 (4.4)	< 2.
3C 319	< 0.3	< 0.2	< 0.3	< 0.12	< 0.7	< 1.0	0.31 (0.12)
3C 321	< 1.8	< 1.5	< 1.1	1.44(0.39)	< 7.	61. (11.)	6. (2.)
3C 346	< 0.18	< 0.3	< 0.10	< 0.15	< 0.4	< 1.1	< 0.3
3C 381	< 1.5	< 1.2	< 0.3	< 0.2	< 1.0	3.8 (1.0)	1.2 (0.2)
3C 382	< 0.4	< 0.6	< 0.4	< 0.7	< 2.	< 6.	< 2.
3C 388	< 0.2	< 0.3	< 0.17	< 0.2	< 0.9	< 1.1	< 0.6
3C 390.3	< 0.9	< 0.6	< 0.3	0.24(0.09)	< 1.8	14.1 (1.5)	< 2.
3C 401	< 0.4	< 0.2	< 0.11	< 0.13	< 0.7	< 1.1	< 0.4
3C 445	< 1.8	< 1.9	< 1.6	< 0.8	< 4.	7.5 (3.6)	< 3.
3C 452	< 0.5	< 0.3	< 0.3	< 0.18	< 1.5	3.2 (1.7)	< 1.2
3C 459	< 2.6	< 1.1	0.94(0.34)	< 0.4	9.6 (2.1)	15.0 (1.3)	9.6 (0.6)
Pic A	< 0.3	< 0.7	< 0.7	< 0.7	< 6.	< 8.	< 1.6

NOTE. — H₂ pure rotational line and PAH fluxes (10^{-14} erg s⁻¹ cm⁻²) or 2σ upper limits measured with *Spitzer* IRS, with 1σ uncertainties in parentheses.

^a The 3C 264 H₂ S(1) line is only a marginal detection (2.3σ), so this source does not meet our H₂ detection criterion of 2 lines detected at $> 2.5\sigma$.

^b The 3C 234 H₂ S(1) line was unmeasurable owing to a large instrumental noise spike.

TABLE 7
RADIO MOHEG FORBIDDEN EMISSION LINES

Source	[Fe II] 5.34 μm	[Ar II] 6.99 μm	[Ar III] 8.99 μm	[S IV] 10.51 μm	[Ne II] 12.81 μm	[Cl II] 14.37 μm	[Ne III] 15.56 μm	[S III] 18.71 μm	[O IV] 25.89 μm	[S III] 33.48 μm	[Si II] 34.82 μm
3C 31	0.48(0.18)	1.3 (0.2)	< 0.3	0.51(0.18)	3.0 (0.2)	< 0.4	1.5 (0.2)	0.73(0.17)	1.1 (0.2)	0.84(0.15)	2.4 (0.3)
3C 84	10. (1.)	12.4(0.9)	2.5 (0.8)	1.4 (0.6)	43.3 (0.5)	6.8 (1.7)	26. (2.)	13. (2.)	< 7.	23. (2.)	62.3 (0.6)
3C 218	0.14(0.05)	0.46(0.07)	< 0.3	< 0.2	1.78(0.08)	< 0.5	0.78(0.17)	< 0.5	1.0 (0.2)	0.93(0.26)	...
3C 270	< 0.8	2.4 (0.3)	0.23(0.10)	0.33(0.08)	4.20(0.08)	0.58(0.20)	2.3 (0.1)	0.87(0.11)	1.3 (0.3)	1.3 (0.2)	2.9 (0.1)
3C 272.1	< 1.5	3.8 (0.6)	< 0.6	1.0 (0.2)	5.6 (0.2)	0.44(0.20)	5.7 (0.2)	3.4 (0.2)	1.4 (0.2)	4.1 (0.1)	11.7 (0.3)
3C 293	1.3 (0.2)	1.9 (0.2)	0.61(0.09)	< 0.3	5.24(0.08)	< 0.3	2.6 (0.1)	1.2 (0.2)	1.5 (0.1)	2.8 (0.3)	...
3C 310	< 0.2	< 0.3	0.09(0.04)	< 0.08	0.28(0.04)	< 0.2	0.47(0.06)	< 0.2	< 0.2	1.1 (0.2)	...
3C 315	0.28(0.11)	0.53(0.14)	0.12(0.04)	0.10(0.04)	0.29(0.05)	< 0.2	0.30(0.09)	< 0.3	0.24(0.08)
3C 317	< 0.3	0.65(0.13)	0.21(0.05)	< 0.08	0.88(0.05)	0.19(0.07)	0.43(0.07)	0.37(0.07)	0.26(0.08)	< 0.3	1.3 (0.2)
3C 326 N	0.23(0.08)	< 0.3	0.30(0.05)	0.09(0.04)	0.44(0.05)	0.17(0.05)	< 0.2	< 0.2	0.12(0.05)
3C 338	< 0.3	< 0.4	< 0.2	0.22(0.11)	0.66(0.11)	< 0.2	0.27(0.07)	< 0.3	0.34(0.10)	0.58(0.16)	1.2 (0.3)
3C 386	0.43(0.08)	< 0.2	< 0.1	< 0.1	0.39(0.04)	0.13(0.06)	0.61(0.05)	0.39(0.10)	< 0.3	0.96(0.21)	2.9 (0.2)
3C 405	2.3 (0.9)	11.6 (0.8)	4.4 (0.7)	16.2 (0.7)	21.7 (0.7)	5.4 (0.4)	47.9 (0.5)	24.2 (0.6)	78.5 (0.7)	29. (1.)	...
3C 424	0.15(0.05)	< 0.07	< 0.09	< 0.07	0.25(0.08)	0.12(0.06)	0.16(0.05)	< 0.2	0.18(0.06)
3C 433	< 0.6	1.3 (0.4)	1.5 (0.2)	1.7 (0.2)	2.6 (0.2)	< 0.9	5.7 (0.2)	0.89(0.20)	7.0 (0.4)
3C 436	< 0.2	< 0.1	0.12(0.05)	0.12(0.04)	0.29(0.10)	< 0.3	0.85(0.10)	0.28(0.11)	0.93(0.12)
Cen A	< 18.	67. (4.)	10.9 (5.2)	28.(4.)	213.(4.)	37. (12.)	233.(18.)	87. (9.)	155. (18.)	264.(11.)	561.(14.)

NOTE. — Flux (10^{-14} erg s^{-1} cm^{-2}) or 2σ upper limit measured with *Spitzer* IRS, with 1σ uncertainties in parentheses.

TABLE 8
HIGH-IONIZATION FORBIDDEN EMISSION LINES

Source	[Ne vi] 7.65	[Ne v] 14.3	[Ne v] 24.31
3C 405	13. (1.)	20.5(0.5)	24.3(0.6)
3C 433	2.3(0.4)	0.8(0.2)	0.9(0.3)
3C 436	0.23(0.05)	< 0.3	< 0.2
Cen A	29.(14.)	37.(11.)	65.(31.)

NOTE. — Flux (10^{-14} erg s $^{-1}$ cm $^{-2}$) measured with *Spitzer* IRS, with 1σ uncertainties in parentheses.

TABLE 9
RADIO MOHEG CONTINUUM AND LINE LUMINOSITIES

Source	$\log \nu L_\nu(178 \text{ MHz})$	$\log \nu L_\nu(24 \mu\text{m}, L_\odot)$	$\log L(\text{H}_2)^{\text{a}}$	$\log L_X(2\text{-}10 \text{ keV})^{\text{b}}$
3C 31	40.33	8.63	40.32	40.67
3C 84	40.92	10.84	41.75	42.91
3C 218	42.46	9.34	41.10	41.69
3C 270	40.07	8.23	39.26	41.08
3C 272.1	39.02	7.42	38.86	39.34
3C 293	41.07	9.74	41.76	42.78
3C 310	41.87	8.64	40.85	...
3C 315	42.02	9.43	41.76	41.68 ^c
3C 317	41.42	8.61	40.53	41.30
3C 326 N	41.90	8.57	41.73	40.63 ^c
3C 338	41.28	8.49	40.54	40.30
3C 386	40.48	7.75	39.87	39.75 ^c
3C 405	44.10	11.31	41.75	44.28
3C 424	42.08	9.53	41.97	...
3C 433	42.46	11.15	42.13	43.90 ^c
3C 436	42.67	10.32	42.31	43.53
Cen A	40.12	9.07	39.88	41.70

^a Observed H₂ rotational line luminosity (erg s $^{-1}$), summed over the 0-0 S(0)-S(3) transitions (Table 4). Corrections of 6-33% are made for undetected emission lines, based on H₂ multi-temperature models (§5).

^b Unabsorbed 2-10 keV nuclear X-ray luminosities (erg s $^{-1}$) from Evans et al. (2006), Balmaverde et al. (2006), Hardcastle et al. (2006), McNamara et al. (2000), Pellegrini (2005), and Ueda et al. (2005)

^c Unabsorbed 2-10 keV nuclear X-ray luminosities (erg s $^{-1}$) measured with *Chandra* (Table 10).

TABLE 10
CHANDRA X-RAY DATA AND AGN SPECTRAL MODELS

Source	t (ks)	chip	model	L_X^{a}	Notes
3C 315	7.7	S3	PL	4.8×10^{41}	S/N too low to detect heavily abs. emission
3C 326 N	27.5	I3	PL	4.3×10^{40}	Low S/N
3C 386	29.1	I3	PL	5.6×10^{39}	
3C 433	37.2	S3	PL + abs. PL	8.0×10^{43}	See Miller & Brandt (2009)
Zw 3146	45.6	I3	PL	8.2×10^{42}	Likely contamination from thermal gas

^a Unabsorbed 2-10 keV nuclear X-ray luminosities (erg s $^{-1}$), measured with *Chandra*.

TABLE 11
 H₂ MODEL PARAMETERS

Source	T(K) ^a	Ortho/Para ^b	$N(\text{H}_2)$ ^c	$M(\text{H}_2)$ ^d	$L_{\text{tot}}(\text{H}_2, \text{rot})$ ^e
3C 31	100. (0.)	1.587	8.6E+21	2.3E+08 (1.6E+08,3.1E+08)	5.8E+39
	250. (60.)	2.955	2.3E+20	6.0E+06 (1.8E+06,2.0E+07)	1.6E+40
3C 84	1140. (150.)	3.000	9.5E+17	2.5E+04 (1.5E+04,4.0E+04)	2.3E+40
	150. (20.)	2.464	<3E+22	<8E+08	2.0E+41
3C 218	580. (30.)	3.000	1.7E+20	4.7E+06 (4.0E+06,5.6E+06)	3.8E+41
	1500. (0.)	3.000	3.2E+18	9.0E+04 (8.0E+04,1.0E+05)	2.2E+41
3C 270	100. (10.)	1.654	8.2E+21	2.0E+09 (1.2E+09,3.5E+09)	7.2E+40
	540. (70.)	3.000	4.7E+18	1.2E+06 (7.0E+05,2.0E+06)	8.4E+40
3C 272.1	1500. (0.)	3.000	5.9E+16	1.5E+04 (1.0E+04,2.1E+04)	4.0E+40
	100. (0.)	1.587	<5E+21	<3E+07	6.7E+38
3C 293	400. (70.)	2.999	3.1E+19	1.6E+05 (8.8E+04,2.8E+05)	2.8E+39
	1500. (0.)	3.000	3.3E+17	1.7E+03 (1.4E+03,2.1E+03)	3.9E+39
3C 310	100. (0.)	1.587	6.7E+21	7.9E+06 (5.3E+06,1.2E+07)	1.9E+38
	290. (180.)	2.983	2.7E+19	3.2E+04 (3.4E+03,3.0E+05)	1.5E+38
3C 315	1150. (120.)	3.000	1.9E+18	2.2E+03 (1.5E+03,3.2E+03)	2.0E+39
	100. (0.)	1.587	2.1E+22	3.6E+09 (3.1E+09,4.2E+09)	1.0E+41
3C 317	278. (9.)	2.980	4.8E+20	8.3E+07 (7.0E+07,9.7E+07)	4.1E+41
	1040. (30.)	3.000	3.2E+18	5.4E+05 (4.8E+05,6.2E+05)	4.1E+41
3C 326 N	140. (20.)	2.340	7.1E+20	1.7E+08 (9.0E+07,3.2E+08)	3.4E+40
	640. (160.)	3.000	1.7E+18	4.1E+05 (2.1E+05,8.0E+05)	5.7E+40
3C 326 N	1500. (0.)	3.000	1.1E+17	2.7E+04 (1.9E+04,3.8E+04)	7.4E+40
	160. (40.)	2.603	<4E+20	<3E+08	1.8E+41
3C 338	330. (40.)	2.994	3.6E+19	3.1E+07 (1.4E+07,7.0E+07)	3.8E+41
	1500. (0.)	3.000	1.6E+17	1.4E+05 (1.1E+05,1.7E+05)	4.6E+41
3C 386	100. (0.)	1.587	<2E+21	<2E+08	4.3E+39
	300. (40.)	2.988	3.4E+19	3.5E+06 (2.2E+06,5.5E+06)	2.2E+40
3C 405	1220. (150.)	3.000	4.3E+17	4.4E+04 (3.0E+04,6.7E+04)	5.7E+40
	110. (10.)	1.751	3.7E+21	2.2E+09 (1.3E+09,3.8E+09)	1.1E+41
3C 424	430. (60.)	3.000	1.9E+19	1.2E+07 (7.7E+06,1.7E+07)	3.9E+41
	1110. (250.)	3.000	5.6E+17	3.4E+05 (1.2E+05,9.7E+05)	3.8E+41
3C 433	100. (0.)	1.587	<3E+21	<2E+08	6.6E+39
	480. (60.)	3.000	9.4E+18	7.6E+05 (5.1E+05,1.1E+06)	3.3E+40
3C 436	1450. (590.)	3.000	<1E+17	<1E+04	2.2E+40
	130. (20.)	2.124	<2E+21	<4E+07	3.9E+39
3C 436	430. (150.)	3.000	5.2E+18	1.4E+05 (2.8E+04,6.4E+05)	3.6E+39
	1500. (0.)	3.000	2.1E+17	5.5E+03 (4.6E+03,6.5E+03)	1.3E+40
3C 436	100. (0.)	1.587	< 2E+22	<4E+09	1.2E+41
	460. (70.)	3.000	4.5E+19	1.2E+07 (6.8E+06,2.1E+07)	4.6E+41
3C 436	1500. (0.)	3.000	1.8E+18	4.6E+05 (3.9E+05,5.3E+05)	1.3E+42
	132. (8.)	2.237	2.9E+21	3.3E+09 (2.4E+09,4.4E+09)	6.5E+41
3C 436	360. (60.)	2.997	1.6E+19	1.8E+07 (8.5E+06,4.0E+07)	3.4E+41
	1340. (230.)	3.000	2.0E+17	2.2E+05 (1.2E+05,4.3E+05)	5.4E+41
3C 436	100. (0.)	1.587	3.1E+22	2.3E+10 (1.9E+10,2.8E+10)	8.3E+41
	350. (80.)	2.996	4.2E+19	3.2E+07 (1.4E+07,7.4E+07)	4.7E+41
3C 436	1300. (210.)	3.000	9.3E+17	7.1E+05 (3.9E+05,1.3E+06)	1.4E+42
	100. (0.)	1.587	6.2E+21	1.6E+10 (1.1E+10,2.4E+10)	8.6E+41
3C 436	300. (40.)	2.987	2.9E+19	7.6E+07 (4.1E+07,1.4E+08)	8.6E+41
	1500. (0.)	3.000	2.0E+17	5.2E+05 (4.3E+05,6.4E+05)	2.5E+42
Cen A	100. (0.)	1.587	1.1E+23	3.4E+07 (1.9E+07,5.9E+07)	8.2E+38
	290. (30.)	2.986	5.0E+21	1.6E+06 (1.1E+06,2.3E+06)	8.0E+39
	1500. (0.)	3.000	9.6E+18	3.0E+03 (2.7E+03,3.4E+03)	6.7E+39

^a H₂ model component temperatures. A temperature range of $100 < T < 1500$ K was enforced in fitting the models. Temperatures pegged at either end of this range have indeterminate uncertainties.

^b Ratio of ortho (odd J) to para (even J) H₂, fit self-consistently to match the thermal equilibrium value.

^c H₂ model column densities (cm^{-2}), assuming a source size of $3''7 \times 3''7$, matching the SL slit width.

^d H₂ model masses and 1σ mass ranges (M_{\odot}).

^e H₂ model luminosities (erg s^{-1}), summed over all pure-rotational transitions. Note that not all of these transitions are directly observed by *Spitzer*.

TABLE 12
RADIO MOHEG H₂ AND DUST MASSES

Source	$M(\text{warm H}_2)^a$	$M(\text{cold H}_2)^b$	warm/cold ^c	Ref. ^d	M_{dust}^e
3C 31	2.4E+08	1.3E+09	0.18	4	2.0E+05
3C 84	4.8E+06-8E+08	2.2E+09	< 0.36	5	4.0E+05
3C 218	2.0E+09	2.0E+09	1.0	2	...
3C 270	1.6E+05-3E+07	<9E+07	...	8	1.0E+03
3C 272.1	7.9E+06	3.7E+06:	2.1:	8	4.0E+03
3C 293	3.7E+09	2.3E+10	0.16	1	2.0E+06
3C 310	1.7E+08
3C 315	3.1E+07-3E+08	1.3E+05
3C 317	3.5E+06-2E+08
3C 326 N	2.2E+09	1.7E+09	1.3	9	...
3C 338	7.6E+05-2E+08	<1E+09	...	2	1.3E+05
3C 386	1.5E+05-4E+07	2.2E+08	< 0.18	8	...
3C 405	1.2E+07-4E+09	<1E+09	...	3	...
3C 424	3.3E+09	< 6E+09	>0.6	6	...
3C 433	2.3E+10	< 9E+09	>3	3	5.0E+05
3C 436	1.6E+10
Cen A	3.6E+07	<3E+08 ^f	>0.12	7	5.0E+05

^a Total mass (M_{\odot}) of warm H₂ components from Table 11. Mass ranges are given for galaxies that are undetected in H₂ S(0) but detected in other H₂ rotational lines, since this line determines our estimate of the mass of the coldest and typically most massive warm H₂ component.

^b Cold H₂ mass (M_{\odot}), estimated from CO flux density and corrected to the same standard Galactic CO conversion factor of $4.6 M_{\odot}/(\text{K km s}^{-1} \text{ pc}^2)$. Upper limits may be underestimated in the case of broad CO lines. Tentative (low S/N) detections are indicated by a colon.

^c Ratio of cols. 2 and 3.

^d Cold H₂ Refs: 1) Evans et al. (1999) 2) Salome & Combes (2003) 3) Evans et al. (2005) 4) Okuda et al. (2005) 5) Salome et al. (2006) 6) Saripalli & Mack (2007), 7) Israel et al. (1990) 8) Ocana Flacquer et al. (2010) 9) Nesvadba et al. (2010).

^e Mass (M_{\odot}) of clumpy dust estimated from optical absorption (De Koff et al. 2000). This could be much less than the amount of dust associated with the warm H₂ or CO, which might be revealed with sensitive far-IR continuum measurements.

^f Cen A cold H₂ mass detected within 40" aperture.

TABLE 13
STAR FORMATION RATES

Source	SFR(PAH 7.7)	SFR(PAH 11.3)
3C 31	0.43 (0.01)	0.78 (0.01)
3C 84	0.71 (0.05)	1.35 (0.03)
3C 218	0.62 (0.09)	1.49 (0.07)
3C 270	0.013 (0.002)	0.021 (0.001)
3C 272.1	0.0036 (0.0007)	0.019 (0.001)
3C 293	1.47 (0.06)	4.81 (0.06)
3C 310	< 0.06	0.068 (0.020)
3C 315	0.67 (0.19)	2.1 (0.1)
3C 317	< 0.03	0.055 (0.009)
3C 326 N	< 0.07	0.27 (0.06)
3C 338	< 0.04	0.10 (0.02)
3C 386	< 0.008	0.017 (0.002)
3C 405	< 1.	< 1.9
3C 424	< 0.16	0.42 (0.08)
3C 433	1.3 (0.6)	2.2 (0.5)
3C 436	2.6 (1.3)	3.5 (1.3)
Cen A	0.048 (0.004)	0.27 (0.01)

NOTE. — Star formation rates ($M_{\odot} \text{ yr}^{-1}$) are estimated from $\text{SFR}(\text{PAH } 7.7) = 2.4 \times 10^{-9} L(\text{PAH}7.7)/L_{\odot}$ and $\text{SFR}(\text{PAH } 11.3) = 9.2 \times 10^{-9} L(\text{PAH}11.3)/L_{\odot}$, using PAH luminosities inside the *Spitzer* IRS SL slit. $\text{SFR}(\text{PAH } 11.3)$ should be considered an upper limit for sources with high (> 0.26) 11.3/7.7 PAH ratio.

TABLE 14
JET CAVITY POWER

Source	Cluster	P(jet cavity) ^a	L(H ₂)/P(jet cavity) ^b
3C 84	Perseus A	1.4E+44	2.7E-03
3C 218	Hydra A	4.3E+44	3.4E-04
3C 272.1	M84, Virgo	1.0E+42	1.1E-03
3C 317	A2052	1.5E+44	2.3E-04
3C 338	A2199	2.7E+44	1.2E-04
3C 405	Cyg A	1.3E+45	3.8E-04

^a Jet cavity power estimated from the $4pV$ enthalpy required to inflate the cavity, divided by the cavity buoyancy timescale (Rafferty et al. 2006).

^b Ratio of H₂ pure rotational line luminosity (summed over 0-0 S(0)-S(3)) to jet cavity power.